Journal of Atmospheric and Solar-Terrestrial Physics 179 (2018) 342–357

Contents lists available at ScienceDirect

Journal of Atmospheric and Solar-Terrestrial Physics

journal homepage: www.elsevier.com/locate/jastp

Atmospheric gravity wave ray tracing: Ordinary and extraordinary waves

R. Michael Jones*, Alfred J. Bedard

Cooperative Institute for Research in Environmental Sciences, University of Colorado, Boulder, CO, 80309-0216, USA

ARTICLE INFO

Keywords:
Internal gravity waves
Dispersion relation
Hamiltonian ray tracing

ABSTRACT

Calculation of internal gravity-wave ray paths in the atmosphere using a general three-dimensional ray tracing computer program is discussed. To initialize a ray-path calculation, it is necessary to specify the initial values for the components of the wave vector at the source so that the dispersion relation is satisfied. For acoustic waves, or for gravity waves in the absence of wind, there is no ambiguity in determining the magnitude of the wave vector once the frequency and direction of propagation (wave-normal direction) have been specified. For gravity waves with wind, however, it is necessary to solve a quartic equation to specify the magnitude of the wavenumber. Two of the roots of the quartic reduce to the usual solutions in the absence of wind, and we designate these roots as 'ordinary waves.' The two new roots (whose values approach infinity as the wind speed approaches zero), we designate as 'extraordinary waves.' A section contrasts the properties of the different gravity wave types.

Comparison with some previously published examples of ray-path calculations of gravity waves shows that those previous examples were actually extraordinary waves, but their significance was not recognized at that time.

In the absence of wind, gravity waves are restricted to a fan of propagation directions centered about horizontal propagation, but asymptotic gravity waves (in the Bousinesq approximation) have a fixed propagation direction for a given frequency. In the presence of a horizontal wind, however, the wave-normal direction is restricted to a fan of directions in the upwind direction, but not in the downwind direction. The ray direction for upwind propagation has no restrictions. A short review of gravity wave theory and the gravity wave dispersion relation is included.

1. Introduction

Gravity waves are ubiquitous in the atmosphere because they are generated by earthquakes, tsunamis, volcanic eruptions, severe storms, and nuclear explosions, in addition to less spectacular mechanisms (e.g. situations where the Richardson number is less than 1/4). See, for example, the work by Stenflo (1986, 1987, 1991, 1996); Stenflo and Stepanyants (1995); Jurén and Stenflo (1973) and the review by Fritts and Alexander (2003, 2012). Section 2 reviews the broad range of atmospheric gravity wave generation mechanisms and their areas of practical impacts.

Atmospheric gravity waves can be detected directly using arrays of pressure sensors (e.g. Liu et al., 1982; Bedard, 1984; Bedard et al., 2004; Bedard, 1982) or can be detected indirectly by using Lidar measurements of temperature profiles (e.g. Chen et al., 2013, 2016; Zhao et al., 2017; Chu et al., 2018) or by measuring the effects of gravity waves in the ionosphere (Nekrasov et al., 1995; Rolland et al., 2010; Makela et al., 2011; Hickey et al., 2009; Artru et al., 2005) or troposphere (Arai et al., 2011; Hickey et al., 2009). Gravity waves can also be detected by radar, rocket soundings, and satellites. In the case of gravity wave propagation to the ionosphere, it is necessary to consider the effect of the Earth's magnetic field (Nekrasov et al., 1992, 1995; Pokhotelov et al., 1994, 1996, 1998; Chmyrev et al., 1991; Streltsov et al., 1990) and to use a dispersion relation for magneto-acoustic-gravity waves (Ostrovsky, 2008; Jones et al., 2017).

Determining the sources of atmospheric gravity waves and understanding how atmospheric gravity waves are generated by their sources is an area of active research. Using ray tracing to help interpret the propagation of gravity waves helps in that endeavor and in part has motivated our work. For example, we are using ray tracing to help interpret the gravity waves observed by Lidar measurements of temperature profiles in Antarctica (Chen et al., 2013, 2016; Zhao et al., 2017).

Section 3 discusses ray tracing, including giving the dispersion relation we used in our ray path calculations. Section 4 shows propagation effects of the Acoustic cutoff frequency and the Brunt-Väisälä frequency. Section 5 discusses non-asymptotic gravity waves. Section 6 shows how the ray tracing program calculates the magnitude of the

* Corresponding author.
E-mail address: michael.jones@colorado.edu (R.M. Jones).

https://doi.org/10.1016/j.jastp.2018.08.014
Received 14 May 2018; Received in revised form 6 August 2018; Accepted 27 August 2018
Available online 30 August 2018

wave vector to initialize the calculation of a ray path. In the presence of wind, there is an additional difficulty in initializing wavenumber, because in the presence of wind there are two types of waves, which we refer to as “ordinary” and “extraordinary.” Section 7 shows dispersion-relation diagrams for gravity waves with and without wind. The dispersion-relation diagrams for the extraordinary waves are very different from those for the ordinary waves. Section 8 shows the effect of including wind on the propagation of gravity waves. Extraordinary wave ray paths are very different from those for ordinary waves. Section 9 compares our ray path calculations and analysis with gravity-wave ray-path calculations of others. We show that some previously published examples of gravity-wave ray paths are actually extraordinary waves. Section 10 discusses properties of various gravity wave types. Section 11 discusses meteorological applications of a gravity wave ray tracing program. Section 12 gives some concluding remarks.

2. Impact areas of atmospheric gravity waves

The areas listed below, with examples, reflect the broad impacts of atmospheric gravity waves in terms of being generated by a rich variety of phenomena, initiating geophysical events, and transferring energy, permitting interactions between the lithosphere, atmospheric layers and the ionosphere. In addition, gravity waves can provide information for warning of the existence of potential hazards (e.g. aircraft turbulence, tsunamis). The lower atmospheric boundary layer involves interacting wind shears, thermal plumes, turbulence, and gravity waves-combining in complex interactions. At times lower level wind shear, instabilities, and gravity waves can produce the erosion of ground based inversions. In other situations thermal plumes can dominate the boundary layer. During the nocturnal boundary layer gravity waves can control the near surface dynamics.

In addition, many major field experiments have measured the properties of atmospheric gravity waves using combinations of remotes sensors and aircraft probes. The DEEPWAVE program (Fritts et al., 2016) is a recent example of an extensive effort to define gravity wave sources and effects in the lower and middle atmosphere. Gravity wave ray trace programs could have a role in helping to guide aircraft and remote sensing measurements. Also, there exist large regional scale efforts to apply high density surface arrays e.g. the USARRAY (Tytell et al., 2016) and also global arrays designed as part of an International Monitoring System (IMS) for monitoring nuclear explosions (Christie and Campus, 2009). Both these arrays have the ability to measure atmospheric gravity wave induced pressure changes. Gravity wave ray tracing can assist in the interpretation of surface array pressure measurements that can provide azimuth and phase speed information.

2.1. Examples of gravity wave generation processes

- Convection (Deardorff et al., 1969; Vadas and Fritts, 2009; Alexander, 1996; Choi et al., 2009; Fovell et al., 1992)
- Severe weather (Bowman and Bedard, 1971; Balachandran, 1980; Curry and Murty, 1974; Nicholls and Pielke, 1994a; b; Taylor and Hapgood, 1988; Dewan et al., 1998; Koch and Siedlarz, 1999)
- Large explosions, volcanoes (ReVelle, 2009)
- Mountain waves (Schoeberl, 1985; Eckermann and Preusse, 1999; Lott and Millet, 2009)
- Terrain forcing (Nappo, 2002)
- Sudden stratospheric warming (Gerrard et al., 2011)
- Fronts (Wrasse et al., 2006; Lin and Zhang, 2008; Plougonven and Zhang, 2014)
- Jets (Suzuki et al., 2013)
- Sea wave forcing (Vadas et al., 2015)
- Geomagnetic activity (Chimonas and Hines, 1970; Testud, 1970)
- Solar eclipse (Chimonas and Hines, 1970)

2.2. Examples of gravity waves in the atmospheric boundary layer

- Gravity waves associated with wind shear induced instabilities (Pramitha et al., 2015)
- Gravity waves associated with temperature inversions (Williams et al., 2002; Bedard et al., 1981; Cunningham and Bedard, 1993)
- Gravity waves associated with the atmospheric boundary layer (Einaudi et al., 1989)
- Gravity waves and boundary layer rolls (Li et al., 2013)
- Gravity waves associated with convective plumes (Vadas and Fritts, 2009)

2.3. Examples of gravity wave initiation of geophysical events

- Severe storm initiation (Uccelini, 1975; Su and Zhai, 2017)
- Sea surface excitation (Šepić et al., 2015)
- Aircraft turbulence (Bedard et al., 1986)
- Modulation of gust surges (Belušić et al., 2004)

2.4. Examples of gravity wave energy transfer

- Atmospheric general circulation models (Lott and Millet, 2009; Alexander et al., 2010; Kim et al., 2003)
- Convectively generated gravity waves (Alexander, 1996)

2.5. Examples of possible gravity wave applications for hazard warning and characterization

- Earthquakes (Mikumo and Watada, 2009)
- Tsunamis (Mikumo and Watada, 2009)
- Meterological Tsunamis (Šepić et al., 2015)
- Earthquake precursors (Lognonné, 2009)
- Tropical Cyclones (Hung and Kuo, 1978; Hung and Smith, 1978; Kim et al., 2009; Hoffmann et al., 2018; Tratt et al., 2018)
- Tornadic storms (Hung et al., 1979)
- Aircraft turbulence (Bedard et al., 1986)

2.6. Examples of gravity waves affecting the middle atmosphere

- (Baumgarten, 2010; Dörnbrack et al., 2017; Gerrard et al., 2004; Krisch et al., 2017)

3. Ray tracing

Ray tracing is a practical method for calculating the ray-theory or WKB approximation for the propagation of waves in a specified medium. Jones (1996, 2007) reviews the conditions for the validity of ray theory and the WKB approximation. Simple tests based on the wavelength of the waves are often inaccurate estimates for the validity of the WKB approximation.

Ray tracing has been used for many years to calculate the propagation of internal gravity waves in the atmosphere (e.g. Eckermann, 1992; Shutts, 1998; Broad, 1999). The propagation of gravity waves in the atmosphere can be calculated using a ray tracing program based on Hamilton's equations (e.g. Slater and Frank, 1947, p. 74) if the dispersion relation is used as the Hamiltonian. The usual barotropic dispersion relation for acoustic-gravity waves (which includes both acoustic and gravity waves) is (Eckart, 1960, eq. (51-2), p. 125) (Gossard and Hooke, 1975, eq. (23-7), p. 112).

$$(\omega_i^2 - 4\Omega_z^2)\left(k_z^2 + \mathbf{k}_A^2 - \frac{\omega_i^2}{C^2}\right) - (k_x^2 + k_y^2)(N^2 - \omega_i^2) = 0\,, \tag{1}$$

where[1]

[1] Equation (2) is consistent with $\mathbf{k}_A \equiv \nabla\rho/(2\rho)$, where ρ is density.

$$k_A^2 = \frac{\omega_a^2}{C^2} = \frac{N^2}{C^2} + \Gamma^2 = \frac{1}{4H^2}, \tag{2}$$

H is the density scale height, N is the Brunt-Väisälä frequency, C is sound speed, ω_a is the acoustic cutoff frequency, $\Gamma \equiv \nabla\rho/(2\rho) - \nabla p/(\rho C^2)$ is the vector generalization of Eckart's coefficient, ρ is density, p is pressure,

$$\omega_i = \omega - \mathbf{k}\cdot\mathbf{U} = \omega - Ck\alpha \tag{3}$$

is the intrinsic frequency, where $\alpha \equiv \mathbf{k}\cdot\mathbf{U}/(Ck)$ is a dimensionless variable that gives the effect of the wind and wave-normal direction relative to the wind direction. ω is the wave frequency, $\mathbf{U}$ is the background wind velocity, $\mathbf{k}$ is the wavenumber, k_z is its vertical component, k_x and k_y are its horizontal components, and Ω_z is the vertical component of the Earth's angular velocity.

The dispersion relation (1) applies to any perfect fluid, such as the ocean or atmosphere. It applies to acoustic waves when the intrinsic frequency ω_i is above the acoustic cutoff frequency ω_a (where compressibility is the dominant restoring force), and to internal gravity waves when the intrinsic frequency ω_i is below the Brunt-Väisälä frequency N (where buoyancy from the Earth's gravitational field is the dominant restoring force).

There is a frequency gap between those two frequencies where all waves are evanescent. Because gravity waves and acoustic waves are separated by a frequency gap, it is always clear how to distinguish between an acoustic wave and a gravity wave. If the intrinsic frequency is above the acoustic cutoff frequency, then it is an acoustic wave. If the intrinsic frequency is below the Brunt-Väisälä frequency, then it is a gravity wave. This is true, even though gravity waves close to the Brunt-Väisälä frequency have some effect from compressibility as a restoring force and acoustic waves near the acoustic cutoff frequency have some effect from gravity as a restoring force. Nearly all of the waves considered here are gravity waves. The dispersion relation (1) can be generalized to include baroclinicity (Jones, 2001, 2012), vorticity, and rate-of-strain (Jones, 2005, 2008a; 2006, 2008b). Even though the dispersion relation (1) is locally isothermal, it is the correct dispersion relation to be used in a ray-tracing program for calculating WKB approximations to the appropriate wave equation (Weinberg, 1962).

For pure gravity waves, we could neglect the ω_i^2/C^2 term in (1) to give (Eckermann, 1997, eq. 26) (Fritts and Alexander, 2003, eq. 23)

$$(\omega_i^2 - 4\Omega_z^2)(k_z^2 + \mathbf{k}_A^2) - (k_x^2 + k_y^2)(N^2 - \omega_i^2) = 0\,. \tag{4}$$

In the ray path calculations presented here, however, we neglect instead the Coriolis term in (1) and set the Hamiltonian H equal to the dispersion relation to give (Hines, 1960, eqs. (21) and (21′))

$$H = \omega_i^2\left(k_z^2 + \mathbf{k}_A^2 - \frac{\omega_i^2}{C^2}\right) - (k_x^2 + k_y^2)(N^2 - \omega_i^2) = 0\,. \tag{5}$$

The Hamiltonian H depends implicitly on position and time through the dependence of temperature, pressure, density, etc. on position and time. In addition, the Hamiltonian depends explicitly on the frequency and components of the wave vector $\mathbf{k}$. The ray path is then calculated using Hamilton's equations. Hamilton's equations in Cartesian coordinates in four spacetime dimensions are:

$$\frac{dx_i}{d\tau} = \frac{\partial H}{\partial k_i}\,,\ i = 1 \to 3, \tag{6}$$

$$\frac{dt}{d\tau} = -\frac{\partial H}{\partial \omega}\,, \tag{7}$$

$$\frac{dk_i}{d\tau} = -\frac{\partial H}{\partial x_i}\,,\ i = 1 \to 3,\ \text{and} \tag{8}$$

$$\frac{d\omega}{d\tau} = \frac{\partial H}{\partial t}\,. \tag{9}$$

Equation (6) gives the progression of the ray. Equation (7) gives the pulse travel time. Equation (8) gives refraction of the ray by changing the components of the wave vector $\mathbf{k}$. Equation (9) gives the frequency shift of the ray due to propagating in a time-varying medium. The meaning of the parameter τ depends on the particular version of the dispersion relation used for the Hamiltonian. Hamilton's equations guarantee that the Hamiltonian (and therefore, the dispersion relation) will remain unchanged along the ray path. The CIRES/NOAA ray tracing program uses Hamilton's equations in Earth-centered spherical polar coordinates.

Examination of (5) shows that in the absence of wind, wave-normal propagation directions for gravity waves (that is for frequencies below the Brunt-Väisälä frequency) are restricted to the fan of angles that are less than $\cos^{-1}\omega_i/N$ from the horizontal. This can be seen qualitatively in Figs. 9 and 10 in Hines (1960).

For pure gravity waves, we can neglect the ω_i^2/C^2 term in (5), and in addition, if we make the Bousinesq approximation by neglecting the $\mathbf{k}_A^2$ term, we get (Hines, 1960, eq. 33)

$$\omega_i^2 k_z^2 - (k_x^2 + k_y^2)(N^2 - \omega_i^2) = 0\,. \tag{10}$$

Equation (10) is an approximate dispersion relation for gravity waves that are usually called asymptotic gravity waves. As can be seen, asymptotic gravity waves have wave-normal directions only at $\pm\cos^{-1}\omega_i/N$ from the horizontal. Whereas asymptotic gravity waves have a fixed propagation direction for a given frequency, gravity waves in general are restricted only to a fan of propagation directions.

An asymptotic gravity wave interpretation of the sequence of arrival and frequencies of ionospheric disturbances from a nuclear explosion is consistent with many observations (Hines, 1967). Chang (1972) verified the use of Hines asymptotic approximation for gravity waves associated with traveling ionospheric disturbances. In addition, laboratory measurements (Mowbray and Rarity, 1967) verified that asymptotic gravity waves are directed to higher elevation angles as the wave frequency approaches the Brunt-Väisälä frequency. In their experiments the wavelengths of the waves generated were approximately the scale of the diameter of the cylindrical driver. Additional experiments (e.g. McLaren et al., 1973; Hurley, 1969) verified the results of Mowbray and Rarity (1967). In all these experiments data were taken at essentially a single wavelength. A range of wavelengths at a given frequency is possible for asymptotic gravity wave generation. The excitation of asymptotic gravity waves can occur over a wide range of atmospheric forcing function scale sizes and can explain why it is often applied in analyzing measurements and model computations.

However, because there are many situations where the asymptotic approximation is not valid, the calculations here use (5) for the dispersion relation. The CIRES/NOAA acoustic-gravity wave ray tracing computer program used for these calculations is a general three-dimensional ray tracing program for calculating acoustic-gravity waves in the atmosphere (described in Bedard and Jones, 2013; Jones and Bedard, 2015) based on an earlier program HARPA for calculating the propagation of acoustic waves (Jones et al., 1986a; b; Georges et al., 1990). The ray tracing program calculates ray paths by integrating Hamilton's equations in Earth-centered spherical polar coordinates (Jones et al., 1986a, pp. 89–91).

Jones (1996) reviews the practical aspects of ray tracing, the WKB approximation, and the limits of geometrical optics to calculate wave propagation in the atmosphere. Although the WKB approximation was given its present name after 1926 (Wentzel, 1926; Kramers, 1926; Brillouin, 1926), the method was discovered earlier (Liouville, 1836, 1837a, 1837b; Rayleigh (John William Strutt), 1912; Jeffreys, 1923).

There are several ray tracing programs for calculating the propagation of acoustic and/or gravity waves (e.g., Marks and Eckermann, 1995; Preusse et al., 2008; Muraschko et al., 2013; Cowling et al., 1971; Broutman et al., 2004; Georges, 1971; Vadas and Fritts, 2009), including some programs that can calculate the effects of winds and dissipation.

There are several ways to initialize the ray parameters at the source, and all of the ways are equally valid, with it being purely a personal choice to choose one method over another.

- In the CIRES/NOAA ray tracing program, the user chooses the frequency and wave-normal direction, and the program uses the dispersion relation to determine the magnitude of the wave number k.
- Another possibility (possibly used by some ray tracing programs) is to choose the frequency and horizontal components of the wave number $\mathbf{k}$, and let the program determine the vertical component of the wavenumber from the dispersion relation.
- Still another possibility (Georges, 1971) is to choose the wave-normal direction and the magnitude of the wave number k or total wavelength, and let the program determine the frequency from the dispersion relation. Section 9 shows that the ray paths Georges (1971) gave as examples are what we here classify as "extraordinary rays." The ordinary and extraordinary waves referred to here are not related to the "ordinary viscous waves" or the "extraordinary viscous waves" referred to by Volland (1969), Hickey and Cole (1987), or Ma (2016).

Jones (1969) points out a distinction between gravity waves that are propagating and gravity waves that are merely advected with the mean wind. Marks and Eckermann (1995) use their ray tracing program to compare turbulent diffusivity with scale-dependent infrared radiative damping. Preusse et al. (2009) compare their ray path calculations with measured global maps of gravity waves. Vadas and Fritts (2005) and Vadas (2007) include damping effects of kinematic viscosity and thermal diffusivity in the thermosphere in their ray path calculations. Vadas and Fritts (2009) use ray tracing to reconstruct the gravity wave field from convective plumes. Ding et al. (2003) include viscosity and thermal conductivity in their ray path calculations. Although the dispersion relation for acoustic-gravity waves is not unique, the resulting WKB approximations from using the various dispersion relations will differ by an amount that is less than the error in the WKB approximations (Einaudi and Hines, 1970; Weinberg, 1962; Jones, 2006). A ray will pass through a critical layer whenever the phase velocity equals the wind velocity, which is equivalent to the intrinsic frequency passing through zero. Booker and Bretherton (1967) show that waves passing through a critical level are attenuated by an amount that depends on the Richardson number. None of the ray paths in the examples presented here passed through a critical level.

4. Acoustic cutoff frequency and Brunt-Väisälä frequency

To illustrate the effect of the Acoustic cutoff frequency and Brunt-Väisälä frequency on propagation, we consider some examples.

The acoustic cutoff frequency profile and Brunt-Väisälä frequency profile are determined indirectly by the temperature profile, and directly by the pressure and density profiles. The latter are determined from the temperature profile through the equation of state and hydrostatic equilibrium.

As an example, we use the temperature profile in Fig. 1, but if we were making ray-path calculations to interpret measurements, we would use more realistic models such as those available from the NRLMSISE-00 Atmosphere Model (NRLMSISE-00, Community Coordinated Modeling Center, 2016) or from measurements (e.g. Chu et al., 2011). For the temperature profile in Fig. 1, we get the acoustic cutoff frequency profile shown in Fig. 2, and the Brunt-Väisälä frequency profile shown in Fig. 3. Combining Figs. 2 and 3 illustrates the frequency gap shown in Fig. 4.

Fig. 4 shows that a frequency of 0.0032 Hz should be above the acoustic cutoff frequency at a height of 10 km. Confirming that, Fig. 5 shows that 0.0032 Hz waves launched at that height are reflected a little below 11 km. These are acoustic waves.

Fig. 4 also shows that a frequency of 0.00249 Hz should be below

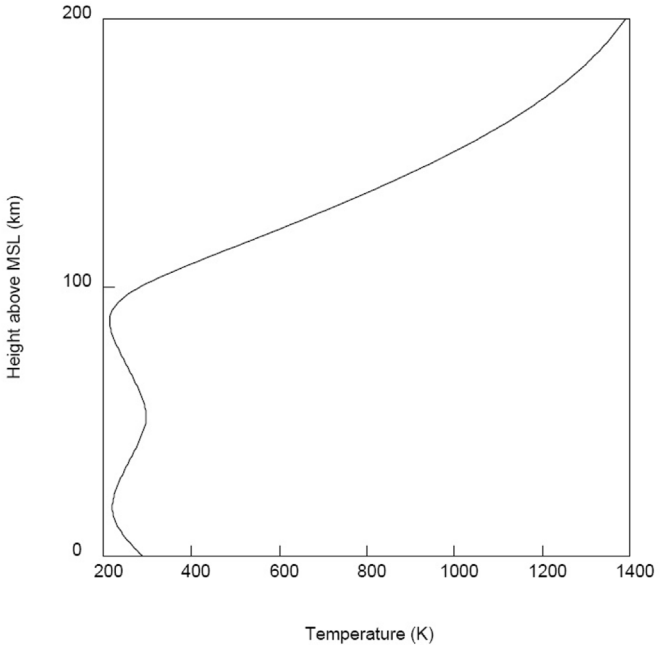

Fig. 1. 1962 Standard Atmosphere temperature profile used for all of the ray-path calculations presented here except for the calculations used for comparison with other work in Fig. 18 and 19. For these calculations, we had no longitude or latitude dependence of temperature.

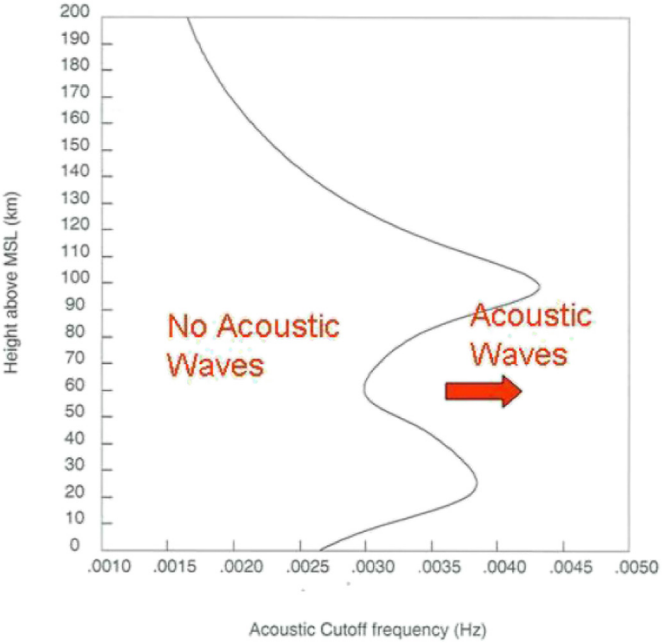

Fig. 2. Acoustic cutoff frequency profile from the temperature profile in Fig. 1. The acoustic cutoff frequency, ω_a, is calculated from $\omega_a = Ck_A = C|\nabla\rho|/(2\rho)$, where C is sound speed, and ρ is density (Jones, 2005, 2006).

the Brunt-Väisälä frequency between the heights of about 10 and 60 km. Confirming that, Fig. 6 shows that a 0.00249 Hz wave is ducted between those two heights. This is a gravity wave. Only one gravity wave is shown here, because other wave-normal directions (outside of only a very narrow range) correspond to waves whose frequency is greater than the Brunt-Väisälä frequency, and are therefore evanescent at the source. We would see more waves propagate if we were to lower the frequency. The ray in Fig. 6 represents a guided gravity wave that is trapped in the 10-to-60-km height range.

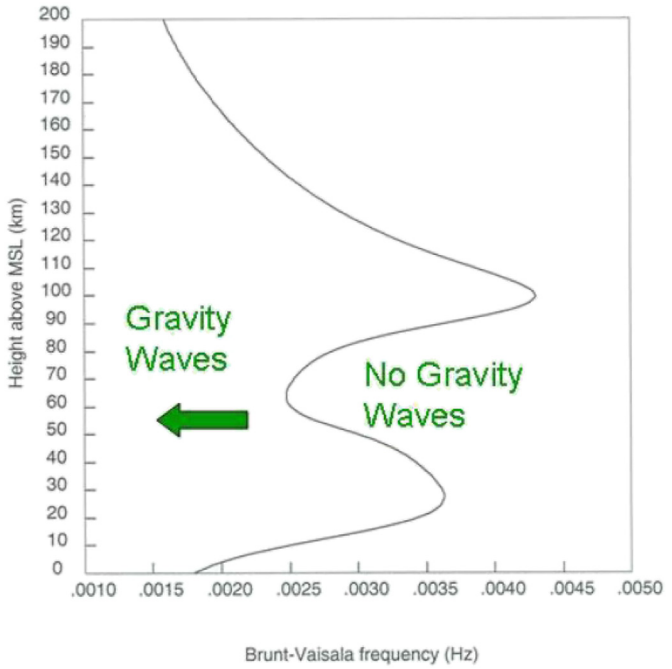

Fig. 3. Brunt-Väisälä frequency profile from the temperature profile in Fig. 1. For the general case of a perfect fluid, such as the ocean or the atmosphere, the Brunt-Väisälä frequency, N, is given by $N^2 = \tilde{\mathbf{g}}\cdot\nabla\tilde{\rho}_{\text{pot}}/\rho = \tilde{\mathbf{g}}\cdot(\nabla\rho - \nabla p/C^2)/\rho$, where $\tilde{\rho}_{\text{pot}}$ is local potential density, ρ is density, p is pressure, C is sound speed, and $\tilde{\mathbf{g}} = \nabla p/\rho$ is the effective acceleration due to gravity (Jones, 2005, 2006). For the special case of the atmosphere, N is also given by $N^2 = -\tilde{\mathbf{g}}\cdot\nabla\theta/\theta$, where θ is potential temperature.

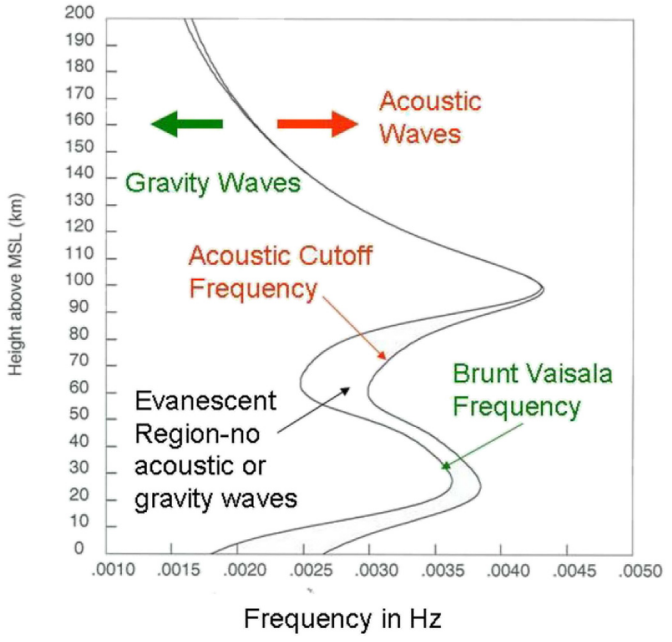

Fig. 4. Acoustic cutoff frequency and Brunt-Väisälä frequency profiles from the temperature profile in Fig. 1.

Fig. 7 gives an example of a lower frequency (0.00125 Hz) where gravity waves for a larger range of transmission directions can propagate. The source is at a height of 5 km. The elevation angle of transmission is stepped from 10° degrees to 90° in steps of 5°, but waves for elevation angles of transmission of 55° and higher are evanescent. The rays for which transmission is possible correspond to wave-normal directions that are less than $\cos^{-1}\omega_i/N$ from the horizontal. That the

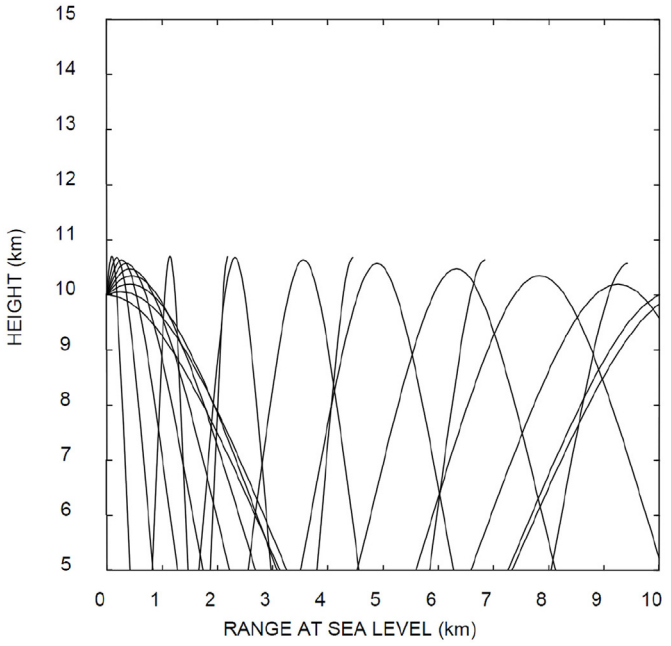

Fig. 5. Acoustic waves, f = 0.0032 Hz (above the acoustic cutoff frequency below about 10.8 km), source height is 10 km. The rays that stop at the top would reflect and return to the ground if we had continued the ray-path calculations.

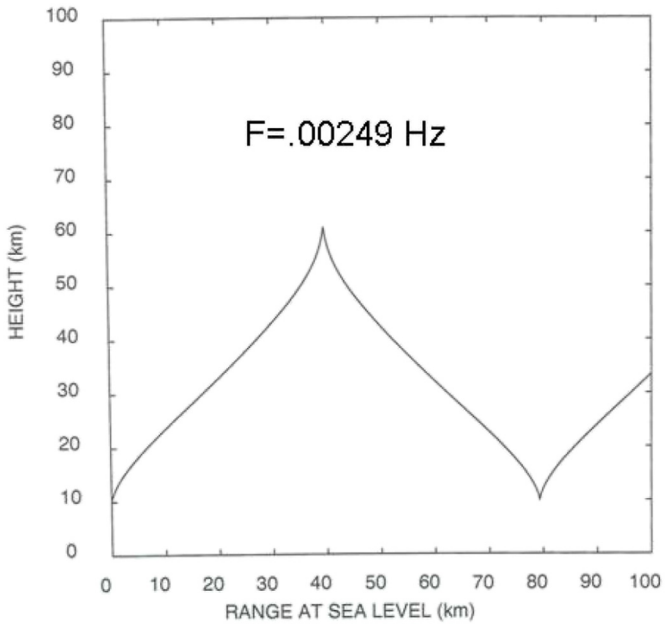

Fig. 6. Gravity wave, f = 0.00249 Hz, below the Brunt-Väisälä frequency between 10 and 60 km, source height is 10 km. The vertical component of the wave-normal vector is zero at the reflection height. Notice the similarity of the cusps in the ray path with the cusps in the ray paths in Figure 80 of page 336 in Lighthill's book (Lighthill, 1978). Lighthill refers to the reflection height as a "critical level," but uses the terminology "special type of critical level" to refer to what is usually referred to as a "critical level" (i.e., where the phase velocity equals the wind velocity, which is equivalent to the intrinsic frequency passing through zero). Although this gravity wave may not be an asymptotic gravity wave, it becomes an asymptotic gravity wave at the upper and lower reflections points, where the wave-normal direction is nearly horizontal and the ray direction is nearly vertical. Reflection occurs in this case at the heights where the Brunt-Väisälä frequency is nearly equal to the wave frequency.

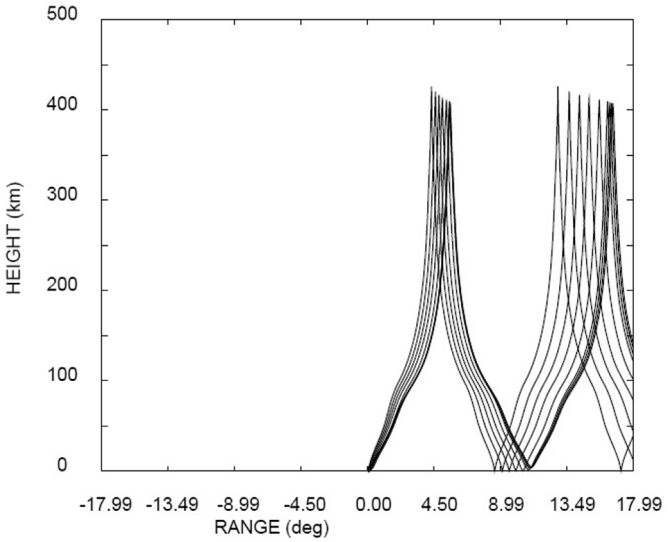

Fig. 7. Gravity waves without wind, f = 0.00125 Hz. Elevation angle of transmission varies from 10° to 50° in steps of 5°. That fan of rays correspond to wave-normal directions that are less than $\cos^{-1}\omega_i/N$ from the horizontal, for which propagation is possible. The waves are evanescent for elevation angles of transmission equal to 55° and above. The source height is 5 km. The distance between tick marks on the horizontal axis is 500 km. The 10° elevation-angle ray reaches an apogee of 407 km at a range of 622 km in 2.35 h, and has a wavelength at the source of 161 km. The 50° elevation-angle ray reaches an apogee of 425 km at a range of 482 km in 5.46 h, and has a wavelength at the source of 44 km. These gravity waves are not asymptotic gravity waves at the source because a fan of wave-normal directions are possible, but they become asymptotic gravity waves at the upper reflections point, where the wave-normal direction is nearly horizontal and the ray direction is nearly vertical. Reflection occurs in these cases at the height where the Brunt-Väisälä frequency is nearly equal to the wave frequency.

wavelengths at the source of the waves in Fig. 7 are large does not necessarily indicate either a breakdown in ray theory or large errors in the WKB approximation. Estimating the errors in the WKB approximation involves locating turning points of the rays, calculating the size of the Airy regions around the turning points, recognizing possible overlaps of Airy regions, and determing if there are any singularities close to turning points (Jones, 1996). Fig. 7 has empty space on the left because we chose to plot Figs. 7, 12 and 13 on the same scale for easy comparison.

5. Non- asymptotic gravity waves

Non-asymptotic waves for a given frequency can be beamed over a range of elevation angles and a fan of angles can result. These occur at the longer wavelength segments of dispersion relation diagrams. Near the nose of the dispersion relation diagrams interactions of the wave normal with the diagram can produce a range of ray directions, limited by the asymptotic approximation angle. Many simulations and measurements of gravity waves above convection and frontal systems have obtained fan-like patterns of launch angles. For example, Holton and Alexander (1999) studied gravity waves in the mesosphere generated by tropospheric convection. They predicted fan-like distributions of gravity waves with higher frequencies at about a 45° launch angle and the lower frequencies at more horizontal launch angles. A broad spectrum of gravity waves was generated from about 20 to 200 km wavelengths and from about 10 to 100 min periods. Wang et al. (2017) in a model simulation of a front system obtained a fan-like pattern of gravity waves propagating in the upstream direction. Fovell et al. (1992) in their model simulations of gravity waves by convection have obtained fans of angles. They applied the asymptotic approximation interpreted as simultaneous forcing at several frequencies to explain their results.

6. Initializing a ray path calculation for a specified frequency and direction of propagation

In the CIRES/NOAA ray tracing program, the user chooses the frequency and wave-normal direction, and the program uses the dispersion relation to determine the magnitude of the wave number ($k = 2\pi/\lambda$) to initialize the ray at the source. In the absence of wind, the dispersion relation (5) gives a simple formula to determine the magnitude of the wave-number. When there is wind, however, the dispersion relation (5) gives a quartic equation to determine the magnitude of the wave-number. It is then necessary to decide which of the four roots of that quartic equation will give the desired ray path. The following discussion addresses that problem, and in the process, finds it useful to differentiate between two kinds of waves, which we refer to as "ordinary" and "extraordinary."

In ray tracing programs that use other methods for initializing a ray-path calculation, it is possible that a quartic equation is not encountered in the initializing process, so that the distinction between the two kinds of waves that we characterize as ordinary and extraordinary was not previously discovered. For example, if the frequency and the horizontal components of the wavenumber are chosen, it is not necessary to solve a quartic equation to initialize the ray path calculation. For pure gravity waves, if the wave-normal direction and the magnitude of the wave-number are chosen, it is also not necessary to solve a quartic equation to initialize the ray path calculation, but for acoustic-gravity waves, it would still be necessary to solve a quartic equation. However, the existence of ordinary and extraordinary gravity waves does not depend on the method of initializing a ray-path calculation, as can be seen from the dispersion-relation diagrams in section 7.

Examination of the dispersion relation (5) shows that the wave-number for acoustic waves varies from zero at the acoustic cutoff frequency to infinity at infinite frequency in the absence of wind. Including wind complicates the situation, as is demonstrated later.

Similarly, the wavenumber for gravity waves varies from a small value to infinity in the absence of wind. Including wind (as will be shown later) separates solutions of the dispersion relation into separate branches, where the wavenumber can be infinite in some branches, but not others.

Substituting (3) into (5) and rearranging terms gives a quartic equation to determine k when given the wave frequency ω and the wave-normal direction.

$$(1-\alpha^2)\alpha^2(Ck)^4 - 2\omega\alpha(1-2\alpha^2)(Ck)^3 + [(1-6\alpha^2)\omega^2 + (\omega_a\alpha)^2 - (k_\perp^2/k^2)N^2](Ck)^2 + 2\omega\alpha(2\omega^2 - \omega_a^2)Ck - \omega^2(\omega^2-\omega_a^2) = 0\,, \quad (11)$$

where $k_\perp^2 \equiv k_x^2 + k_y^2$ is the square of the horizontal component of the wave vector, we have used $k^2 = k_z^2 + k_\perp^2$, $\omega_a = Ck_A$ is the acoustic cutoff frequency, and notice that the quantity $k_\perp^2/k^2$ depends only on the wave-normal direction. Although by definition, k is positive, (11) can have negative roots. The negative roots are referred to here as extraneous roots. The extraneous roots are not physical, and the CIRES/NOAA ray tracing program ignores them. Table 1 summarizes conditions under which various waves are propagating, evanescent, or extraneous. Ray-path calculations are made for only propagating waves.

Eckermann (1997, eq. 29) similarly develops a quartic formula, but for the vertical wavenumber rather than the magnitude of the wave-number, and neglects the acoustic term rather than the Coriolis term, but then makes an approximation to give a quadratic equation.

When calculating ray paths with the CIRES/NOAA ray tracing program, the height, longitude, and latitude of the source, the wave frequency, and the wave-normal direction are specified as input parameters. That determines the coefficients for the quartic equation (11). In addition, we specify in the input data whether we want to calculate an ordinary ray, an extraordinary ray, or one of the four quartic roots as root 1, 2, 3, or 4. The program then solves the quartic equation to find

Table 1
Categories of the roots of the quartic equation that determines the magnitude of the wavenumber. The four roots are assumed to be ordered from left to right in increasing value of the real part of the root. Thus, Root 1 is the largest negative root, while Root 4 is the largest positive root. n_{sol} is the number of real roots. It is clear from Figs. 9–11 that the number of real roots is 2 or 4 and that two roots of the quartic have negative real parts and two roots have positive real parts. When there are only two real roots, propagation in the upwind direction is evanescent, and propagation in the downwind direction is possible only for the two types of extraordinary wave. $\mathbf{k}\cdot\mathbf{u}$ is positive for downwind propagation, negative for upwind propagation. Extraneous roots are roots with negative wavenumber. The extraneous roots are not physical and are not used. The ray tracing program uses the information in this table to decide whether to make a ray-path calculation. The program does not calculate a ray path for extraneous roots or for waves that are evanescent at the transmitter.

n_{sol}	$k\cdot u$	Extraneous Roots (not used)				Wanted Roots			
		(Real part <0)				(Real part >0)			
		Root 1		Root 2		Root 3		Root 4	
		Propagating	Evanescent	Propagating	Evanescent	Propagating	Evanescent	Propagating	Evanescent
4	<0	Large Extraordinary		Ordinary		Ordinary		Small Extraordinary	
2	<0	Large Extraordinary		Small Extraordinary			Ordinary		Small Extraordinary
4	>0	Small Extraordinary		Ordinary		Ordinary		Large Extraordinary	
2	>0		Small Extraordinary		Ordinary	Small Extraordinary		Large Extraordinary	

the four solutions of (11), and chooses (based on the input data)[2] one of those four solutions to begin the ray path calculations. Since the wave-normal direction at the source is known, choosing one of the four values for k allows all three components of the wave vector $\mathbf{k}$ to be determined at the source. From that point on, numerically integrating Hamilton's equations gives the ray location and all three components of the wave vector $\mathbf{k}$ along the ray.

To give insight into the propagation, it is useful to understand the meaning of the four roots of the quartic. Wind speed is normally much smaller than the sound speed C, so that the dimensionless parameter α is also small. By seeing the behavior of the quartic equation as α approaches zero, we can understand the significance of the four roots. More detail is given in subsections 6.1, 6.2, and 6.3.

6.1. Ordinary waves

All of the ray path calculations presented here use the full dispersion relation (5), which is then equivalent to (11). However, we here make some approximations to (11) to give insight into the nature of the ordinary and extraordinary waves.

We define an ordinary wave as the wave that would exist in the absence of wind. Therefore, to find approximate roots of (11) for the ordinary wave for small wind speed, we neglect terms in (11) that would not contribute to approximate solutions of (11) to first order. This gives a quadratic equation to give an approximate formula for k:

$$\left[\omega^2 - \frac{k_\perp^2}{k^2}N^2\left(1 + \frac{2Ck\alpha}{\omega}\right)\right](Ck)^2 + 2\omega^3\alpha Ck - \omega^2(\omega^2 - \omega_a^2) \approx 0\,. \tag{12}$$

An approximate solution of (12) to lowest order in α is

$$k \approx \frac{\omega}{C}\sqrt{\frac{\omega^2 - \omega_a^2}{\omega^2 - \frac{k_\perp^2}{k^2}N^2}} - \frac{\omega\alpha}{C}\frac{\omega^4 - \frac{k_\perp^2}{k^2}N^2(2\omega^2 - \omega_a^2)}{\left(\omega^2 - \frac{k_\perp^2}{k^2}N^2\right)^2}\,. \tag{13}$$

The CIRES/NOAA ray tracing program uses a numerical solution of the full quartic equation (11) to initialize a ray path calculation. The ray tracing program does not use the approximate formula (12) at all. Equation (12) is used here only to give insight into the propagation.

[2] Specifically, a value of 1, 2, 3, or 4 for the value of a particular input parameter means to choose root 1, 2, 3, or 4, a value of zero for that parameter means to choose a root that corresponds to an ordinary wave, a value of −1 for that parameter means to choose the root that corresponds to a small extraordinary wave, and a value of −2 for that parameter means to choose the root that corresponds to a large extraordinary wave.

6.2. Extraordinary waves

The wavenumbers for the extraordinary wave are the large roots of the quartic equation (11). For these large roots, we look for solutions where $Ck\alpha$ is finite as α approaches zero. To first order in α, only the first three terms in (11) contribute to the solution for finite $Ck\alpha$. To show that, we divide (11) by $(Ck)^2$ to give

$$\begin{aligned}&(1-\alpha^2)(Ck\alpha)^2 - 2\omega(1-2\alpha^2)(Ck\alpha)\\ &+ [(1-6\alpha^2)\omega^2 + (\omega_a\alpha)^2 - (k_\perp^2/k^2)N^2]\\ &+ \alpha^2[2\omega(2\omega^2 - \omega_a^2)Ck\alpha - \omega^2(\omega^2 - \omega_a^2)]/(Ck\alpha)^2\\ &= 0\,.\end{aligned} \tag{14}$$

To find an approximate solution of (14) for $Ck\alpha$ to first order in α, we neglect α^2 in (14) to give

$$(Ck\alpha)^2 - 2\omega(Ck\alpha) + [\omega^2 - (k_\perp^2/k^2)N^2] \approx 0\,. \tag{15}$$

Equation (15) has the solutions

$$k \approx \frac{\omega \pm (k_\perp/k)N}{C\alpha} = \frac{\omega \pm (k_\perp/k)N}{\mathbf{k}\cdot\mathbf{U}/k}\,. \tag{16}$$

Notice that these two roots approach infinity as the wind speed approaches zero.[3] (That is, the wavelength approaches zero as the wind speed approaches zero.) Notice that the intrinsic frequency for the solution given in (16) is given by $\omega_i = \mp(k_\perp/k)N$. That corresponds to an asymptotic gravity wave, which explains why there are no extraordinary acoustic waves. To find the next order approximate solution of (14) for small α, we could substitute the solution in (16) back into the last term in (14), and again solve the resulting quadratic equation in $Ck\alpha$.

The CIRES/NOAA ray tracing program uses a numerical solution of the full quartic equation (11) to initialize a ray path calculation. The ray tracing program does not use the approximate formula (16) at all. Equation (16) is used here only to give insight into the propagation.

For the case where the wind is horizontal and the azimuth direction of propagation is exactly upwind or downwind, we can write (16) as

$$k = \frac{\omega \pm N(k_\perp/k)}{Uk_\perp/k}\,. \tag{17}$$

For downwind propagation at an angle θ from the horizontal, this gives

$$k = \frac{\omega \pm N\cos\theta}{U\cos\theta}\,, \tag{18}$$

[3] However, when the wind speed equals zero, these two roots disappear because (11) then changes from a quartic equation to a quadratic equation.

where the upper sign corresponds to the large extraordinary ray, and lower sign corresponds to the small extraordinary ray. For upwind propagation at an angle θ from the horizontal, this gives

$$k = \frac{\omega \mp N \cos\theta}{-U \cos\theta}, \tag{19}$$

where the upper sign corresponds to the small extraordinary ray, and lower sign corresponds to the extraneous large extraordinary ray.

6.3. Gravity waves

To give further insight into the properties of extraordinary waves, we consider the special case of gravity waves. To neglect acoustic waves, we neglect the ω_i^2/C^2 term in (5). Neglecting that term, we substitute (3) into (5) and rearrange terms to give a quartic equation to determine k when given the wave frequency ω and the wave-normal direction. This gives

$$\begin{aligned}&\alpha^2(Ck)^4 - 2\alpha\omega(Ck)^3\\ &- [(k_\perp^2/k^2)N^2 - \omega^2 - \alpha^2\omega_a^2](Ck)^2\\ &- 2\alpha\omega\omega_a^2 Ck + \omega^2\omega_a^2 = 0\,.\end{aligned} \tag{20}$$

We can factor (20) to first order in α to give

$$\begin{aligned}&\left\{Ck - \frac{\omega\omega_a}{\sqrt{N^2k_\perp^2/k^2 - \omega^2}} + \frac{\alpha\omega_a^2\omega N^2k_\perp^2/k^2}{(N^2k_\perp^2/k^2 - \omega^2)^2}\right\} \times \left\{Ck + \frac{\omega\omega_a}{\sqrt{N^2k_\perp^2/k^2 - \omega^2}} + \frac{\alpha\omega_a^2\omega N^2k_\perp^2/k^2}{(N^2k_\perp^2/k^2 - \omega^2)^2}\right\} \times \{\alpha Ck - \omega - Nk_\perp/k\} \times \{\alpha Ck - \omega + Nk_\perp/k\}\\ &= \alpha^2(Ck)^4 - 2\alpha\omega(Ck)^3 - [(k_\perp^2/k^2)N^2 - \omega^2](Ck)^2 - 2\alpha\omega\omega_a^2 Ck + \omega^2\omega_a^2 + \alpha^2 \text{ terms} + \alpha^3 \text{ terms} = 0\,.\end{aligned} \tag{21}$$

For upwind propagation, the four factors in (21) are respectively the ordinary wave, the extraneous[4] ordinary wave solution, the small extraordinary wave, and the extraneous large extraordinary wave solution. For downwind propagation, the four factors in (21) are respectively the ordinary wave, the extraneous ordinary wave solution, the large extraordinary wave, and the small extraordinary wave.

7. Dispersion-relation diagrams

7.1. Without wind

A graphical representation of a dispersion relation is given by a dispersion-relation diagram. Fig. 8 shows a dispersion-relation diagram without wind. It is a plot of vertical wavenumber on the vertical axis versus horizontal wavenumber on the horizontal axis for a constant frequency. Usually, in calculating a ray path, we choose the source location, the wave frequency, and the wave-normal direction to launch a ray. A straight line from the origin to the dispersion-relation curve gives an allowed wave-normal vector, in which the length of the line gives the wavenumber ($k = 2\pi/\lambda$, where λ is the wavelength), and the direction gives the normal to a wave front (Hines, 1960, Fig. 10). The ray direction (which gives the direction of propagation of a pulse or wave packet) is normal to the dispersion relation curve at that point where the wave-normal vector meets the dispersion-relation curve (Hines, 1960, Fig. 10).

If the angle of the wave-normal direction with the horizontal axis is too large, there will be no intersection with the dispersion-relation curve, indicating that propagation is impossible in that direction (that is, the wave is evanescent in that direction). Rays whose wave-normal direction is asymptotic to the dispersion-relation diagram in Fig. 8 are called asymptotic waves. For asymptotic waves, once the frequency is chosen, there is only one wave-normal direction possible and only one ray direction possible. However, as can be seen from Fig. 8, for non-asymptotic waves there are other wave-normal directions possible, including exactly horizontal propagation. The rays for which transmission is possible correspond to wave-normal directions that are less than $\cos^{-1}\omega_i/N$ from the horizontal.

One example of the simulation of non-asymptotic gravity waves is from the work of Ding et al. (2003). They launched waves with a single period of 30 min, changing phase velocities in presenting a fan of launch angles. In the following sections we will explore the implications of winds on atmospheric gravity waves.

7.2. Including wind

Including wind in the dispersion relation for gravity waves has a profound effect. To see that, we look at the dispersion-relation diagram with wind shown in Fig. 9. Downwind is to the right. The effect of wind is to bring in parts of the diagram on the left and right from infinity. These parts brought in from infinity by the presence of wind, we refer to as extraordinary waves, in analogy with electromagnetic wave propagation in the ionosphere (e.g. Budden, 1961; Ratcliffe, 1962). The separate branch on the downwind (right) side of the diagram, we refer to as the "large[5] extraordinary wave." The other parts of the curve (except the part near the origin), we refer to as the "small[6] extraordinary wave." The curves continue to infinity at the top and bottom of the figure. Whereas propagation upwind (to the left) is still restricted to a fan of wave-normal directions centered about horizontal propagation as in Fig. 8 when there was no wind, wave propagation downwind has no restriction on wave-normal direction.

An expansion of Fig. 9 near the origin is shown in Fig. 10. Propagation upwind (to the left) is restricted to a fan of wave-normal directions centered about horizontal propagation as in Fig. 8 when there was no wind, but ray direction (which is perpendicular to the dispersion-relation curve) can be in any direction for upwind propagation (but some of those ray directions correspond to an ordinary ray). An expansion of Fig. 10 near the origin is shown in Fig. 11, which shows the dispersion relation diagram for the ordinary ray with wind. It is similar to the dispersion relation diagram without wind, but shifted slightly to the right.

For downwind propagation (propagation to the right in Fig. 10) of the small extraordinary wave at an angle θ from the horizontal, the magnitude of k in Fig. 10 is given approximately by taking the lower sign in (18). For upwind propagation (propagation to the left in Fig. 10) of the small extraordinary wave, the magnitude of k in Fig. 10 is given approximately by taking the upper sign in (19). For downwind propagation (propagation to the right in Fig. 9), the magnitude of k for the large extraordinary ray in Fig. 9 is given approximately by taking the upper sign in (18).

As can be seen from Figs. 9–11, a straight line from the origin has the possibility of intersecting the dispersion-relation curve in four places. Thus, choosing the frequency and direction of propagation is not sufficient to determine the wave. It may be necessary to choose the type of wave desired.

For example, choosing a wave-normal direction that is nearly horizontal will give four intersections with the dispersion-relation curve. Two downwind (to the right), and two upwind (to the left). These four intersections correspond to the solutions of the quartic equation (11).

[4] An extraneous solution of the quartic is one in which the magnitude of k is negative. An extraneous solution is not physical.

[5] because these waves have such large wavenumbers.

[6] because these waves have smaller wavenumbers than large extraordinary waves, even though they usually have larger wavenumbers than ordinary waves.

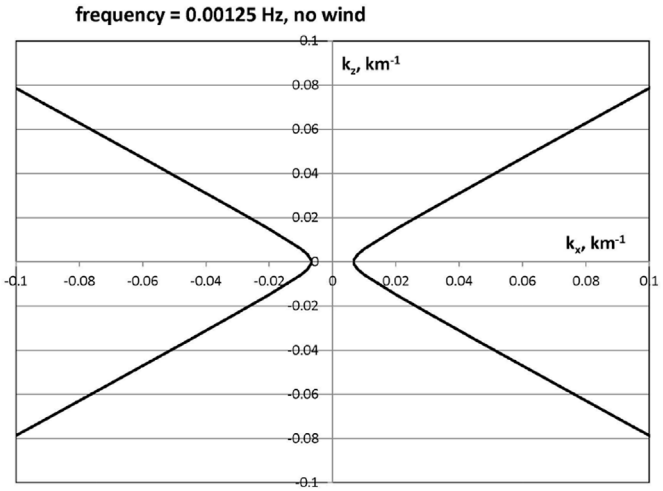

Fig. 8. Dispersion relation diagram without wind, $f = 0.00125$ Hz, $C = 0.3$ km/s, $N = 0.01$ s^{-1}, and $k_A = 0.0267$ km^{-1}. The slope of the asymptotes is determined by the ratio of N to ω. The intersection of the dispersion-relation curve with the horizontal axis is determined by k_A. As can be seen, propagation is confined to wave-normal directions that are confined within a fan of angles that surround horizontal propagation. That fan of rays correspond to wave-normal directions that are less than $\cos^{-1}\omega_i/N$ from the horizontal, for which propagation is possible. Similar gravity-wave dispersion-relation diagrams can be seen for other frequencies in Hines (1960, Fig. 9).

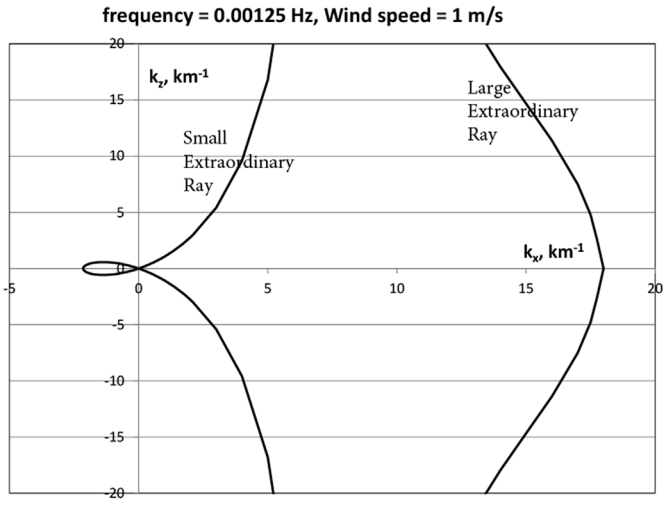

Fig. 9. Dispersion relation diagram showing the small extraordinary ray and the large extraordinary ray with 1 m/s wind blowing to the right. Otherwise, conditions as in Fig. 8. Whereas propagation upwind (to the left) is still restricted to a fan of wave-normal directions centered about horizontal propagation as in Fig. 8 when there was no wind, wave propagation downwind has no restriction on wave-normal direction. There is a critical level (where the intrinsic frequency equals zero) between the small extraordinary ray and the large extraordinary ray as the wavenumber approaches $\pm\infty$ at the top and bottom of the figure. The dispersion relation diagram for the large extraordinary ray crosses the horizontal axis where the intrinsic frequency is the negative of the Brunt-Väisälä frequency. Fig. 10 shows the detail near the origin.

The intersections near the origin give waves that are similar to the no-wind case (one upwind and one downwind), which we refer to as "ordinary waves," in analogy with electromagnetic wave propagation. The other intersection in the downwind direction, we refer to as the "large extraordinary wave," and the other intersection in the upwind direction, we refer to as the "small extraordinary wave."

As we make the wave-normal direction more vertical, we eventually reach a situation in the upwind direction in which the wave-normal

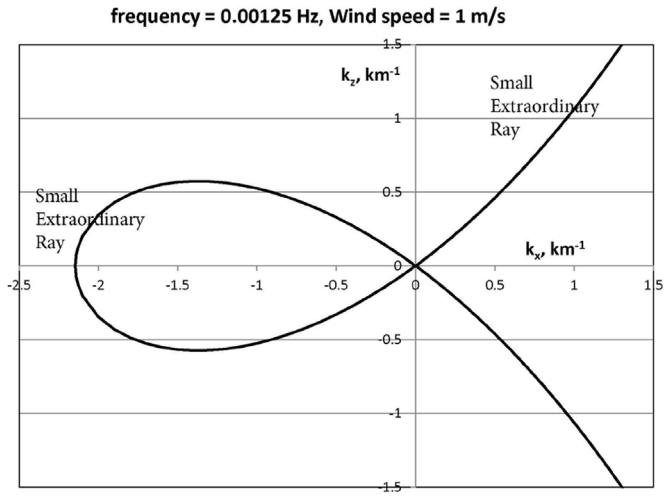

Fig. 10. Dispersion relation diagram showing the small extraordinary ray. Conditions are the same as in Fig. 9. Propagation upwind (to the left) is restricted to a fan of wave-normal directions centered about horizontal propagation as in Fig. 8 when there was no wind, but ray direction (which is perpendicular to the dispersion-relation curve) can be in any direction for upwind propagation (but some of those ray directions correspond to an ordinary ray). There aro no critical levels (where the intrinsic frequency equals zero) in this figure. The dispersion relation diagram for the small extraordinary ray crosses the horizontal axis (on the far left) where the intrinsic frequency equals the Brunt-Väisälä frequency. Fig. 11 shows the detail near the origin.

vector is tangent to the dispersion-relation curve. At that point, the upwind ordinary and extraordinary waves have the same wavenumber, and the resulting ambiguity means that as the wave propagates, what was an ordinary wave may become an extraordinary wave or vise versa. Making the wave-normal direction even more vertical will give no intersection with the dispersion-relation curve in the upwind direction, so that all such waves launched in the upwind direction will be evanescent. In that case, the quartic equation (11) will have only two real roots plus a complex pair.

The slope of the asymptotes in Figs. 8, 10 and 11 is $\sqrt{N^2/\omega^2 - 1}$. If θ is the angle of the wave-normal direction to the horizontal, then we have $\cos\theta = \omega/N$. When there is no wind, Fig. 8 shows that gravity waves will propagate if the wave normal direction is such that the angle relative to horizontal is less than $\cos^{-1}(\omega/N)$. For ordinary waves, Fig. 11 shows that the same is approximately true for ordinary waves. Fig. 10 shows that for upwind propagation, propagation of the small extraordinary wave is also possible if the angle of the wave normal with the horizontal is less than $\cos^{-1}(\omega/N)$. For downwind propagation, Fig. 10 shows that propagation of the small extraordinary wave is possible if the angle of the wave normal with the horizontal is larger than $\cos^{-1}(\omega/N)$. Fig. 9 shows that propagation of the large extraordinary wave is possible only for downwind propagation, and shows that exactly vertical propagation (wave-normal direction) of the large extraordinary wave (or any gravity wave) is not possible. However, exactly vertical propagation of the ray direction for the small extraordinary wave is possible as can be seen in Fig. 10.

8. Ray paths with wind

Including wind alters the gravity-wave ray paths. We demonstrate this using a wind model in which a wind blowing toward the East starts at zero on the ground and increases linearly to 5 m/s at 500 km. As with the no-wind case in Fig. 7, the source is at a height of 5 km, and the elevation angle of transmission is stepped from 10° to 90° in steps of 5°. Although such a simple wind model is not a realistic wind profile, it is useful here to illustrate the effect of wind on ray paths.

The ray paths for transmission downwind and upwind of the

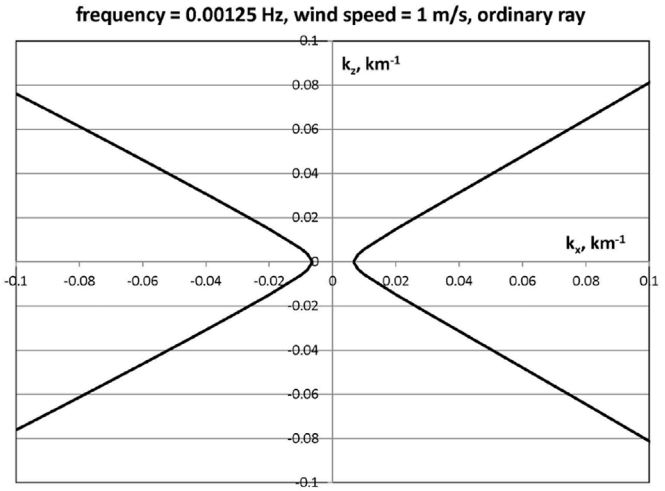

Fig. 11. Dispersion relation diagram for the ordinary ray. Conditions are the same as in Fig. 9. Although this dispersion relation diagram is similar to the no-wind dispersion relation diagram in Fig. 8, it differs greatly far outside the plotting area. There aro no critical levels (where the intrinsic frequency equals zero) in this figure.

"ordinary ray" are shown in Figs. 12 and 13, respectively. Although these ray paths are similar to the no-wind case in Fig. 7, the waves are blown downwind, and the reflection heights differ from the no-wind case in Fig. 7.

Figs. 14 and 15 show downwind and upwind ray paths respectively for the "small extraordinary ray." As can be seen, these rays differ greatly from those of the no-wind case in Fig. 7, and the ordinary waves in Figs. 12 and 13.

Ray paths for the "large extraordinary ray" are not shown because they were not interesting as they stayed within a few kilometers of the ground for these conditions in which the wind speed near the ground

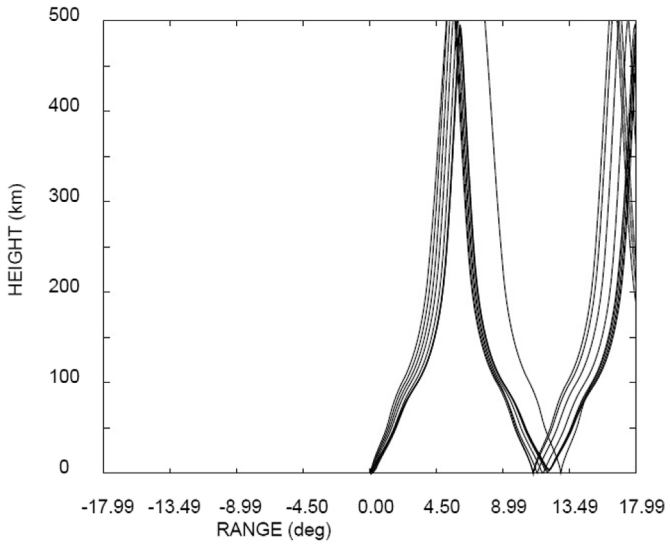

Fig. 12. Ordinary ray, downwind, f = 0.00125 Hz (wind starts at zero on the ground and increases linearly to 5 m/s at 500 km). The source is at a height of 5 km. The elevation angle of transmission is stepped from 10° degrees to 90° in steps of 5°, but waves for elevation angles of transmission of 55° and higher are evanescent. Otherwise, conditions as in Fig. 7. The 10° elevation-angle ray reaches an apogee of 486 km at a range of 689 km in 3 h. The 50° elevation-angle ray reaches an apogee of 709 km at a range of 724 km in 10 h.

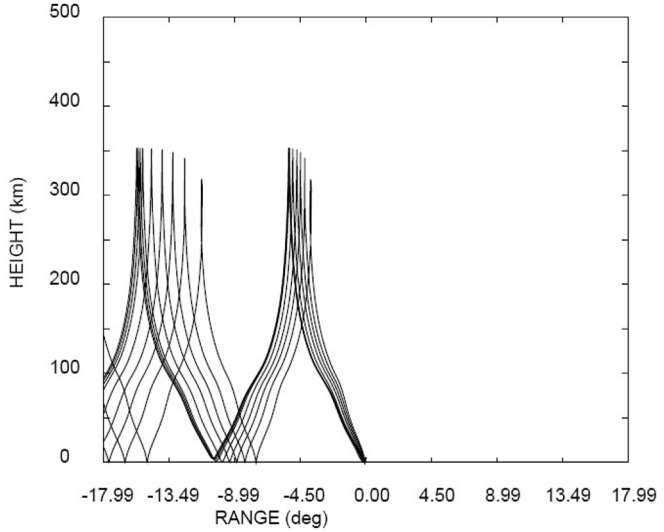

Fig. 13. Ordinary ray, upwind, f = 0.00125 Hz. The source is at a height of 5 km. The elevation angle of transmission is stepped from 10° degrees to 90° in steps of 5°, but waves for elevation angles of transmission of 55° and higher are evanescent. Otherwise, conditions as in Fig. 12. The 10° elevation-angle ray reaches an apogee of 353 km at a range of 589 km in 2 h. The 50° elevation-angle ray reaches an apogee of 318 km at a range of 422 km in 3.6 h.

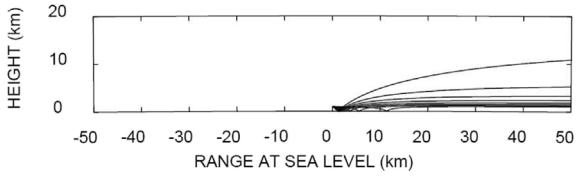

Fig. 14. Small extraordinary ray, downwind, f = 0.00125 Hz. Elevation angle of transmission varies from 50° through 85° in steps of 5°. Rays for elevation angles of transmission of 10° through 45° and 90° were evanescent at the source. The 50° elevation angle of transmission had rays that got the highest and had a pulse travel time of 88 h. The 55° elevation angle of transmission had a pulse travel time of 233 h. The source height is 1 km. Otherwise, conditions as in Fig. 12.

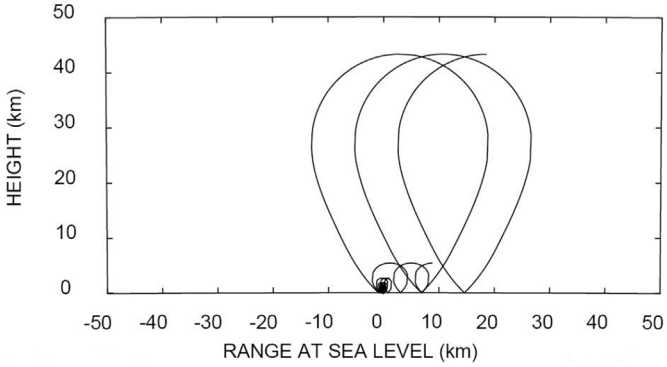

Fig. 15. Small extraordinary ray, upwind, f = 0.00125 Hz. Elevation angle of transmission varies from 10° through 45° in steps of 5°. Rays for elevation angles of 50° through 90° were evanescent at the source. Rays for 45° elevation angles reached the highest and had a pulse travel time of 62 h to the apogee and a total of 122 h from the source back down to the first ground reflection. Rays for 40° elevation angles reached a height of 5.4 km with a pulse travel time of 50 h and a total of 93 h from the source back down to the first ground reflection. Otherwise, conditions as in Fig. 14.

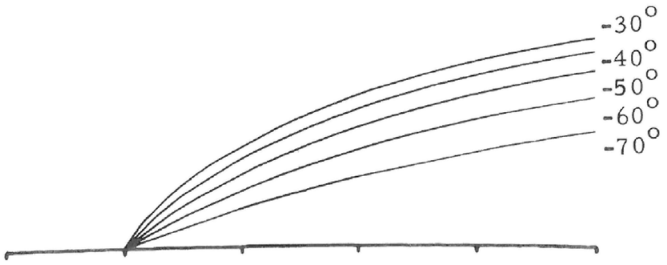

Fig. 16. Ray paths for internal gravity waves, all with a total wavelength of 10 km, as the initial direction of phase propagation (labeled on the curves) is varied. The atmosphere is isothermal and wind increases linearly with height by 0.1 m/s/km, blowing to the right. The scale is 100 km/div. The vertical scale is the same as the horizontal scale. (Georges, 1971, Fig. 4, page 40).

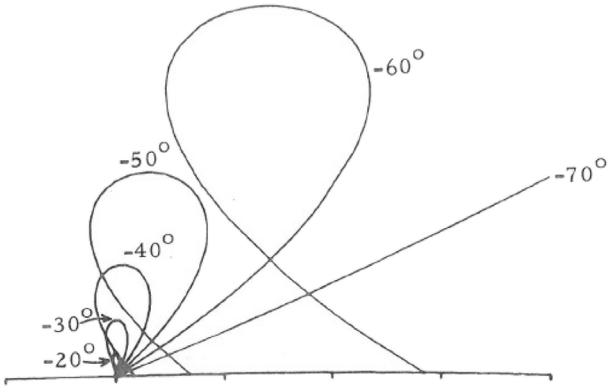

Fig. 17. Ray paths for internal gravity waves, all with a total wavelength of 10 km, as the initial direction of phase propagation (labeled on the curves) is varied. The atmosphere is isothermal and wind increases linearly with height by 0.1 m/s/km, blowing to the left. Otherwise, conditions as in Fig. 16. The scale is 100 km/div. The vertical scale is the same as the horizontal scale (Georges, 1971, Fig. 4, page 40). A similar ray path plot can also be seen as Fig. 63–3 on page 326 in Gossard and Hooke (1975).

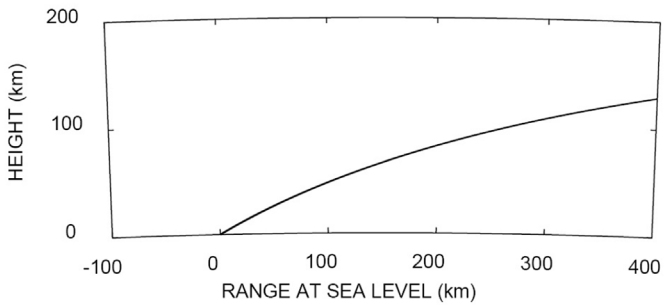

Fig. 18. Ray paths for internal gravity waves, small extraordinary ray, downwind. f = 0.00163946 Hz, λ = 10.0021 km at the source, elevation angle of transmission is ± 60°, source height is 0.5 km. The atmosphere is isothermal and wind increases linearly with height by 0.1 m/s/km. Otherwise, conditions as in Fig. 16. The pulse travel time is about 4.7 h.

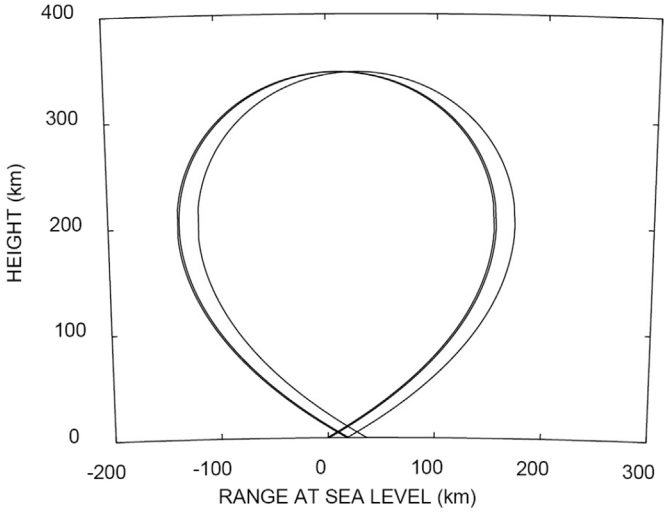

Fig. 19. Ray paths for internal gravity waves, upwind. Small extraordinary wave that began as an ordinary wave. f = 0.00163446 Hz, λ = 9.8 km at the source. Wind is blowing to the left. The atmosphere is isothermal and wind increases linearly with height by 0.1 m/s/km. Otherwise, conditions as in Fig. 18. The pulse travel time is about 6 h from the source to the apogee. The total pulse travel time from the source back down to the first ground reflection is about 10 h.

was so small. For the large extraordinary rays, only rays launched downwind are not evanescent at the source. As can be seen from Fig. 9, large extraordinary rays exist only in the downwind direction.

9. Comparison with other calculations

Comparison with other work is useful to add confidence to the present analysis and to give further insight into the propagation of gravity waves.

Figs. 16 and 17 (Georges, 1971, Fig. 4, page 40) show examples of downwind and upwind propagation, respectively. All of these examples are for a wavelength of 10 km, and various frequencies and elevation angles of transmission. It is clear from comparing Figs. 16 and 17 with Figs. 12–15, that the rays in Figs. 16 and 17 are for "small extraordinary rays," not "ordinary rays."

Because wavelength at the source was specified in Figs. 16 and 17, rather than frequency, each ray path in those two figures for the various elevation angles of transmission has a different frequency. Because those frequencies were not given in the publication (Georges, 1971), we had to experiment by varying frequency until we got a wavelength of 10 km in each of our comparisons. To simplify the comparisons, we decided to make ray path calculations for only the 60° elevation angle of transmission.

Although the source was on the ground in the ray path calculations in Figs. 16 and 17, we chose to move the source slightly off the ground to a height of 0.5 km for our comparisons because the wind speed is zero on the ground for this model, and the "small extraordinary" rays would not exist there when specifying frequency rather than specifying wavenumber.

Figs. 18 and 19 show the comparison ray paths we calculated for an elevation angle of transmission of plus and minus 60°, for both downwind and upwind propagation.

Fig. 18 is for transmitting a small extraordinary ray downwind. The roots of the quartic equation at the source are Ck = 250 $\sec^{-1}$ (large extraordinary wave), 0.19 $\sec^{-1}$ (small extraordinary wave), and $-0.36 \pm 0.79\, i$ $\sec^{-1}$ (evanescent ordinary and small extraordinary waves), where C is the local speed of sound. The calculation is for the small extraordinary wave, and the frequency was adjusted to give a wavelength of about 10 km.

The ray in the upwind case in Fig. 19 starts as an "ordinary ray," but becomes a "small extraordinary ray" at a height of about 3.5 km. The roots of the quartic equation at the source are Ck = 0.88 $\sec^{-1}$ (small extraordinary wave), 0.19 $\sec^{-1}$ (ordinary wave), -0.015 $\sec^{-1}$ (extraneous[7] ordinary wave), and -250 $\sec^{-1}$ (extraneous large extraordinary wave). The calculation is for transmitting an ordinary wave.

[7] An extraneous wave corresponds to a negative value for the magnitude of the wavenumber.

However, something interesting happens to the ray at a height of 3.6975 km. At that height, the roots of the quartic are $Ck = 0.19\ \mathrm{sec}^{-1}$ (small extraordinary wave), $0.19\ \mathrm{sec}^{-1}$ (ordinary wave), $-0.095\ \mathrm{sec}^{-1}$ (extraneous ordinary wave), and $-33\ \mathrm{sec}^{-1}$ (extraneous large extraordinary wave). At that height, the wavenumbers for the ordinary wave and the small extraordinary wave are equal, and the ray tracing program has started to calculate the ray for the small extraordinary wave from this height upward.

At a height of 10 km, the roots of the quartic are $Ck = 0.19\ \mathrm{sec}^{-1}$ (small extraordinary wave), $0.10\ \mathrm{sec}^{-1}$ (ordinary wave), $-0.065\ \mathrm{sec}^{-1}$ (extraneous ordinary wave), and $-12\ \mathrm{sec}^{-1}$ (extraneous large extraordinary wave), and the ray tracing program is integrating a ray for which $Ck = 0.19\ \mathrm{sec}^{-1}$. The ray tracing program uses the quartic only when beginning a ray path calculation for initializing the wavenumber. After that, it uses the roots of the quartic only for comparison to identify what ray is being calculated.

So, the ray path shown in Fig. 19 is mostly a small extraordinary wave that began as an ordinary wave. However, ray identification is difficult when two kinds of rays have nearly equal wavelengths.

The downwind case (Fig. 18) agrees reasonably well with Fig. 16, but the upwind case (Fig. 19) agrees only qualitatively with Fig. 17. The disagreement might be because the source in Figs. 16 and 17 was on the ground (where there was no wind), whereas we put the source at a height of 0.5 km, where it was possible to have an extraordinary wave because there is wind at that height.

Here is the explanation of the upwind ray paths for the small extraordinary wave in Fig. 19 in terms of the dispersion-relation diagram in Fig. 10. Fig. 20 will help that explanation. The curve represents the dispersion-relation diagram for the upwind small extraordinary wave. As the wind speed increases, the dispersion-relation diagram contracts, and as the wind speed decreases, it expands. The source height is 0.5 km. The ray begins as an ordinary ray, but very quickly becomes a small extraordinary ray. Near the ground, the wind speed is very small, so the dispersion relation for the small extraordinary wave in Fig. 10 is expanded out to the left very far. in that case, there is very little difference between the small extraordinary wave and the ordinary wave. We start with the wave-normal direction to be - 60° in the upwind direction. This give a ray direction that is up and also in the upwind direction. This corresponds to the "Starting Point" in Fig. 20.

As the ray moves up, the wind speed increases, and the loop in Fig. 10 for the upwind dispersion-relation diagram in Fig. 10 gets smaller. As the small extraordinary wave propagates, the horizontal component of the wave vector k stays constant because the medium varies only in the vertical direction. To keep the horizontal component of k constant while the dispersion-relation diagram gets smaller, the wave-normal direction must change to be more horizontal. Since the wave normal is pointing downward, it will be pointing less downward. At a certain point, the wave-normal direction will intersect the dispersion-relation diagram at a point where the dispersion relation diagram is horizontal. At that point, the ray direction will be pointing exactly up because the ray direction is perpendicular to the dispersion-relation curve. This corresponds to the lower "Inflection Point" in Fig. 20.

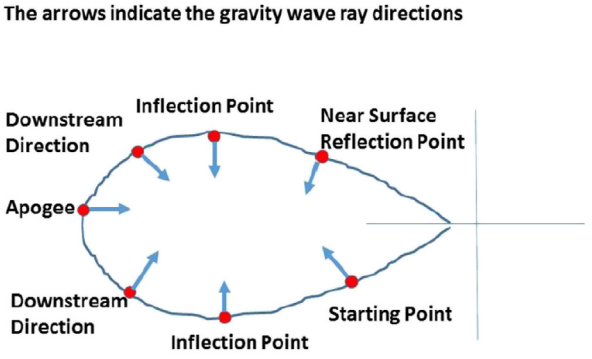

Fig. 20. Dispersion-relation diagram (similar to that in Fig. 10) to help explain upwind propagation of the small extraordinary wave.

As the ray continues upward, the dispersion-relation diagram continues to contract as the wind speed increases, and the wave-normal direction continues to be more horizontal to keep the horizontal component of k constant. At that point, the ray direction is still upward, but the horizontal component of the ray direction is now downwind even though the horizontal component of the wave-normal direction is still upwind. This corresponds to the lower "Downstream Direction" in Fig. 20.

As the ray continues upward, the wind speed continues to increase, and the dispersion relation diagram continues to contract. Eventually, the wave-normal direction becomes horizontal (still in the upwind direction), and the ray direction also becomes horizontal, but in the downwind direction. At that point, the ray is at the apogee, and will begin to come back down. This corresponds to the "Apogee" in Fig. 20.

As the ray starts down, the wind speed decreases, the dispersion-relation diagram expands, and the wave-normal direction moves upward to keep the horizontal component of *k* constant. This corresponds to the upper "Downstream Direction" in Fig. 20.

As the ray continues downward, the wind speed continues to decrease, the dispersion relation diagram continues to expand, and the angle of the wave normal with the horizontal continues to increase, we eventually reach a point where the k vector intersects the dispersion-relation diagram at a point where the dispersion relation diagram is horizontal. At that point, the ray direction is exactly down. This corresponds to the upper "Inflection Point" in Fig. 20.

As the ray continues downward, the wind speed continues to decrease, the dispersion-relation diagram continues to expand, and the angle of the wave normal with the horizontal continues to increase, the ray direction will again be pointing upwind and downward. This corresponds to the "Near Surface Reflection Point" in Fig. 20.

Eventually, the ray gets back to the starting height, then continues downward, where it reflects from the ground, and repeats the cycle. This explains the loops in Fig. 19. The same explanation applies to the ray paths in Fig. 15 as well, except that the ray paths in Fig. 15 are small extraordinary rays throughout, with no coupling from an ordinary ray.

The behavior of the rays for downwind propagation of the small extraordinary ray in Figs. 14 and 18 can be explained similarly in terms of contracting and expanding of the dispersion-relation diagram as the ray moves up or down and the wind speed increases or decreases.

10. Properties of various gravity wave types

The purpose of this section is to summarize the characteristics of various gravity wave types. We envision that in some cases wave properties can overlap making wave types difficult to distinguish. In other situations, the wave types can be clear (e.g. the generation of asymptotic waves at defined frequencies Hines, 1967).

10.1. Asymptotic gravity waves

At a given frequency there is only one propagation direction possible.

At a given frequency a larger range of wavelengths can occur. These will usually be at shorter wavelengths, especially at higher frequencies.

Lower frequencies will produce lower ray elevation propagation angles relative to the surface.

This approximation has been verified to apply in a variety of

situations from laboratory modelling to gravity waves generated by convective processes.

10.2. Non-asymptotic gravity waves

At a given frequency there is a fan of propagation directions possible with the largest angle defined by the asymptotic approximation direction.

For a given frequency a limited range of wavelengths can occur. These will usually be at longer wavelengths, close to the nose of the dispersion diagram.

These will usually occur at lower frequencies (e.g. 6 min period for asymptotic versus 13 min period for non-asymptotic).

10.3. Ordinary gravity waves with winds

The dispersion relation is similar to the dispersion relation for gravity waves without wind.

10.4. Small extraordinary gravity waves

Propagation in the upwind direction is restricted to a fan of wave-normal directions similar to the no-wind situation. Although ray propagation can be in any direction when the wave-normal direction is upwind, some of those ray directions correspond to ordinary waves.

For upwind propagation, propagation of small extraordinary waves is possible if the angle of the wave normal is less than $\cos^{-1}\omega/N$.

For downwind propagation of the small extraordinary gravity wave is possible if the angle of the wave normal with the horizontal is larger than $\cos^{-1}\omega/N$.

For small extraordinary waves there can be large differences between upwind and downwind propagation in contrast to ordinary gravity waves (e.g. Figs. 14 and 15 for small extraordinary waves relative to Figs. 12 and 13 for ordinary gravity waves). The findings of Wang et al. (2017) of gravity waves propagating only in the upstream direction could have been small extraordinary waves.

10.5. Large extraordinary gravity waves

The only restrictions on the wave-normal direction for the large extraordinary waves are that propagation is possible only in the downwind direction and exactly vertical propagation of the large extraordinary gravity wave is not possible. Large extraordinary waves tend to travel at low speeds and be controlled by the wind environment.

If there are significant flows at the initiation point (e.g. a density current moving at 20 m/s), a large extraordinary gravity wave can be embedded in such features and potentially produce significant effects. In such cases the dispersion curve for large extraordinary rays moves closer to the origin. The wave-like disturbances documented by Fulton et al. (1990) moving with an outflow system could have been large extraordinary waves.

11. Examples of possible meteorological application areas of a gravity wave ray trace program

The downdrafts from severe weather produce density currents. These density currents can in turn produce a variety of wave disturbances. Researchers have documented with case studies numbers of situations where atmospheric gravity waves occurred in conjunction with or resulting from density currents. Examples of case studies include the work of Knupp (2006) who performed an observational analysis of a gust front to bora to solitary wave transition within an evolving nocturnal boundary layer. Doviak and Ge (1984) studied an atmospheric solitary wave observed with a Doppler radar, a tall tower, and a surface network. Zhang and Fritsch (1988) documented relationships between Internal gravity waves and a squall line. Fulton et al. (1990) analyzed the Initiation of a solitary wave family in the demise of a nocturnal thunderstorm density current, also showing an example of the waves embedded within the current. Haase and Smith (1984): detail a case study of morning glory wave clouds in Oklahoma.

These observations typically involved extensive observational systems (e.g surface networks, soundings, Doppler radars, Doppler lidars, towers or aircraft). Historically, only very limited numbers of cases were observed in sufficient detail to enable modelling.

We suggest that one valuable application of a gravity wave ray tracing program would be to perform sensitivity studies, for example, varying the height and strength of ground based inversions relative to atmospheric gravity wave propagation characteristics. It will be interesting to determine situations where rays leak out of waveguides to the upper atmosphere resulting in gravity wave dissipation.

Atmospheric gravity waves can have important roles in initiating convection, as well as being initiated by convection. Such meteorological processes could be used to examine possible roles of ordinary and extraordinary gravity waves. If a physical process generates gravity waves, the type of wave created can determine whether or not the possibility of new convection is likely. For example, a downdraft impacting a quiescent environment can only create an ordinary gravity wave. If there is a ground based regional inversion present, energy can be transferred horizontally with minimal loss to the upper atmosphere.

If in contrast, downdrafts descend into existing outflows from previous storms other types of gravity wave initiation are possible. It will be valuable to explore a variety of such situations.

12. Concluding remarks

We have shown that although gravity wave ray tracing has been widely applied, there are some interesting features that add a certain complexity, interest, and difficulty. Choosing the frequency and launch angle (of the wave-normal direction) in the presence of wind gives a quartic equation to determine the wavenumber. This means that in addition to specifying the usual parameters of source location, frequency, and transmission direction, it is necessary to specify what kind of ray one wants (ordinary, small extraordinary, or large extraordinary). Notice that this is analogous to specifying ordinary or extraordinary waves for radio waves in the ionosphere (e.g. Budden, 1961; Ratcliffe, 1962) or characteristic polarization for light waves in birefringent crystals.

The distinction between ordinary and extraordinary gravity waves has apparently not previously been noticed, in spite of the fact that all of the example gravity-wave ray paths presented by Georges (1971) were extraordinary rays.

Although “geometrical phase” (also called “Berry phase” or “additional memory”) (Berry, 1990; Budden and Smith, 1976; Smith, 1975; Weinberg, 1962) can have a noticeable effect on the WKB approximation, including “geometrical phase” does not change the dispersion relation or the ray paths (Weinberg, 1962, Section 4).[8]

The acoustic-cutoff frequency profile and the Brunt-Väisälä frequency profile that result from a given temperature profile can cause interesting ducting of acoustic waves and gravity waves. A wave of a given frequency may be an acoustic wave at some heights but be a gravity wave at some other height.

In the future, we plan to apply the CIRES/NOAA atmospheric gravity wave ray tracing program to meteorological cases where detailed observations are available, such as those in Antarctica (e.g. Chen et al., 2013, 2016; Zhao et al., 2017), or interesting processes have been identified (e.g. leakage of gravity wave energy from ducts formed by ground-based stable layers).

We hope that the gravity wave properties developed and reviewed

[8] Notice that (Weinberg, 1962, eq. 136) is the three-dimensional analog of (Budden and Smith, 1976, eq. 6).

here will be useful to researchers interpreting observations and analytical results.

Acknowledgments

The authors thank William Otto and Wendi Madsen for their assistance in upgrading the ray tracing program to be compatible with present-day compilers and loaders. We thank Emily Gu for help in making many of the calculations presented here. We also acknowledge Xinzhao Chu for discussions on the paper presentation. This research was partially supported by the National Science Foundation (NSF) grants OPP-1246405, OPP-1443726, and AGS-1136272.

References

Alexander, M.J., 1996. A simulated spectrum of convectively generated gravity waves: propagation from the tropopause to the mesopause and effects on the middle atmosphere. J. Geophys. Res. Atmosphere 101 (D1), 1571–1588. https://doi.org/10.1029/95JD02046.

Alexander, M.J., Geller, M., McLandress, C., Polavarapu, S., Preusse, P., Sassi, F., Sato, K., Eckermann, S., Ern, M., Hertzog, A., Kawatani, Y., Pulido, M., Shaw, T., Sigmond, M., Vincent, R., Watanabe, S., July 2010. Recent developments in gravity-wave effects in climate models and the global distribution of gravity-wave momentum flux from observations and models. Q. J. R. Meteorol. Soc. 136, 1103–1124.

Arai, N., Iwakuni, M., Watada, S., Imanishi, Y., Murayama, T., Mogami, M., 2011. Atmospheric boundary waves excited by the tsunami generation related to the 2011 great tohoku-oki earthquake. Geophys. Res. Lett. 38, 1–5. https://doi.org/10.1029/2011GL049146. L00G18.

Artru, J., Ducic, V., Kanamori, H., Lognonné, P., 2005. Ionospheric detection of gravity waves induced by tsunamis. Geophys. J. Int. 160, 840–848. https://doi.org/10.1111/j.1365-246X.2005.0255.x.

Balachandran, N.K., 1980. Gravity waves from thunderstorms. Mon. Weather Rev. 108 (6), 804–816.

Baumgarten, G., 2010. Doppler Rayleigh/mie/Raman lidar for wind and temperature measurements in the middle atmosphere up to 80 km. Atmospheric Measurement Techniques 3 (6), 1509–1518. https://www.atmos-meas-tech.net/3/1509/2010/.

Bedard Jr., A.J., 1982. Sources and detection of atmospheric wind shear. AIAA J. 20, 940–945.

Bedard Jr., A.J., 1984. Optimizing the use of surface sensors for wind shear detection. J. Aircraft 21, 971–977.

Bedard Jr., A.J., Jones, R.M., 2013. Infrasonic ray tracing applied to mesoscale atmospheric structures: refraction by hurricanes. J. Acoust. Soc. Am. 134 (5), 3446–3451.

Bedard Jr., A.J., Nagle, R., LeFebvre, T., 1981. Monostatic acoustic sounder measurements during project AEOLUS 1980: case studies describing the erosion of surface-based stable layers. In: Proceedings, International Symposium on Acoustic Remote Sensing of the Atmosphere and Oceans. June 22-25, 1981. The University of Calgary, Calgary, Alberta, Canada VI-27VI57. Published August 1982.

Bedard Jr., A.J., Canavero, F., Einaudi, F., 1986. Atmospheric gravity waves and aircraft turbulence encounters. J. Atmos. Sci. 43 (23), 2838–2844.

Bedard Jr., A.J., Bartram, B.W., Entwistle, B., Golden, J., Hodanish, S., Jones, R.M., Nishiyama, R.T., Keane, A.N., Mooney, L., Nicholls, M., Szoke, E.J., Thaler, E., Welsh, D.C., 2004. Overview of the ISNet data set and conclusions and recommendations from a march 2003 workshop to review ISNet data. In: Proceedings 22nd Conference on Severe Local Storms. 4-8 October 2004, Hyanis, MA, Sponsored by the Amer. Meteorol. Soc., Boston, MA.

Belušić, D., Pasarić, M., Orlić, M., 2004. Quasi-periodic bora gusts related to the structure of the troposphere. Q. J. R. Meteorol. Soc. 130 (598), 1103–1121. https://doi.org/10.1256/qj.03.53.

Berry, M.V., 1990. Budden & Smith's 'additional memory' and the geometrical phase. Proc. R. Soc. London, Ser. A 431, 531–537.

Booker, J.R., Bretherton, F.P., 1967. The critical layer for internal gravity waves in a shear flow. J. Fluid Mech. 27 (03), 513–539.

Bowman, H.S., Bedard, A.J., 1971. Observations of infrasound and subsonic disturbances related to severe weather. Geophys. J. Roy. Astron. Soc. 26 (1–4), 215–242. https://doi.org/10.1111/j.1365-246X.1971.tb03396.x.

Brillouin, L., 1926. La mécanique ondulatoire de Schrödinger; une méthode générale de résolution par approximations successives. Academie des sciences 183, 24–26 Paris.

Broad, A.S., 1999. Do orographic gravity waves break in flows with uniform wind direction turning with height? Q. J. R. Meteorol. Soc. 125 (557), 1695–1714. https://doi.org/10.1002/qj.49712555711.

Broutman, D., Rottman, J.W., Eckermann, S.D., 2004. Ray methods for internal waves in the atmosphere and ocean. Annu. Rev. Fluid Mech. 36 (1), 233–253. https://doi.org/10.1146/annurev.fluid.36.050802.122022.

Budden, K.G., 1961. Radio Waves in the Ionosphere. University Press, Cambridge.

Budden, K.G., Smith, M.S., 1976. Phase memory and additional memory in WKB solutions for wave propagation in stratified media. Proc. R. Soc. London, Ser. A 350, 27–46.

Chang, N.J.F., 1972. Justification for the use of Hines' "asymptotic relations" for traveling ionospheric disturbances. In: AGARD Conference Proceedings, vol. 115 13,13–1 to 13–8, paper 13.

Chen, C., Chu, X., McDonald, A.J., Vadas, S.L., Yu, Z., Fong, W., Lu, X., 2013. Inertia-gravity waves in Antarctica: a case study using simultaneous lidar and radar measurements at McMurdo/Scott Base (77.8°S, 166.7°E). J. Geophys. Res.: Atmosphere 118 (7), 2794–2808. https://doi.org/10.1002/jgrd.50318.

Chen, C., Chu, X., Zhao, J., Roberts, B.R., Yu, Z., Fong, W., Lu, X., Smith, J.A., 2016. Lidar observations of persistent gravity waves with periods of 3-10 h in the Antarctic middle and upper atmosphere at McMurdo (77.83°S, 166.67°E). J. Geophys. Res.: Space Physics 121 (2), 2015JA022127 1483–1502. https://doi.org/10.1002/2015JA022127.

Chimonas, G., Hines, C.O., 1970. Atmospheric gravity waves induced by a solar eclipse. J. Geophys. Res. 75 (4), 875. https://doi.org/10.1029/JA075i004p00875.

Chmyrev, V., Marchenko, V., Pokhotelov, O., Stenflo, L., Streltsov, A., Steen, Å., 1991. Vortex structures in the ionosphere and the magnetosphere of the earth. Planet. Space Sci. 39 (7) 1025 – IN4.

Choi, H.-J., Chun, H.-Y., Song, I.-S., Apr, 2009. Gravity wave temperature variance calculated using the ray-based spectral parameterization of convective gravity waves and its comparison with Microwave Limb Sounder observations. J. Geophys. Res. B 114 D08111.

Christie, D.R., Campus, P., 2009. The IMS Infrasound Network: Design and Establishment of Infrasound Stations. Springer Netherlands, Dordrecht, pp. 29–75. https://doi.org/10.1007/978-1-4020-9508-5_2.

Chu, X., Yu, Z., Gardner, C.S., Chen, C., Fong, W., 2011. Lidar observations of neutral Fe layers and fast gravity waves in the thermosphere (110-155 km) at McMurdo (77.8°S, 166.7°E), Antarctica. Geophys. Res. Lett. 38 (23) L23807. https://doi.org/10.1029/2011GL050016.

Chu, X., Zhao, J., Lu, X., Harvey, V.L., Jones, R.M., Chen, C., Fong, W., Yu, Z., Roberts, B.R., Dörnbrack, A., 2018. Lidar observations of stratospheric gravity waves from 2011 to 2015 at McMurdo (77.84°S, 166.69°E), Antarctica: Part II. Potential energy densities, lognormal distributions, and seasonal variations. J. Geophys. Res.: Atmosphere 123 (15), 7910–7934. https://agupubs.onlinelibrary.wiley.com/doi/abs/10.1029/2017JD027386.

Cowling, D.H., Webb, H.D., Yeh, K.C., 1971. Group rays of internal gravity waves in a wind-stratified atmosphere. J. Geophys. Res. 76 (1), 213–220. https://doi.org/10.1029/JA076i001p00213.

Cunningham, W.J., Bedard, A.J., 1993. Mountain valley evacuation by upper level flows - a scale model study. AIAA J. 31 (9), 1569–1573. publisher: American Institute of Aeronautics and Astronautics. https://doi.org/10.2514/3.11816.

Curry, M.J., Murty, R.C., 1974. Thunderstorm-generated gravity waves. J. Atmos. Sci. 31 (5), 1402–1408.

Deardorff, J.W., Willis, G.E., Lilly, D.K., 1969. Laboratory investigation of non-steady penetrative convection. J. Fluid Mech. 35, 7–31.

Dewan, E.M., Picard, R.H., O'Neil, R.R., Gardiner, H.A., Gibson, J., Mill, J.D., Richards, E., Kendra, M., Gallery, W.O., 1998. Msx satellite observations of thunderstorm-generated gravity waves in mid-wave infrared images of the upper stratosphere. Geophys. Res. Lett. 25 (7), 939–942. https://agupubs.onlinelibrary.wiley.com/doi/abs/10.1029/98GL00640.

Ding, F., Wan, W., Yuan, H., 2003. The influence of background winds and attenuation on the propagation of atmospheric gravity waves. J. Atmos. Sol. Terr. Phys. 65 (7), 857–869.

Dörnbrack, A., Gisinger, S., Kaifler, B., 2017. On the interpretation of gravity wave measurements by ground-based lidars. Atmosphere 8 (3).

Doviak, R.J., Ge, R., 1984. An atmospheric solitary gust observed with a Doppler radar, a tall tower and a surface network. J. Atmos. Sci. 41 (17), 2559–2573.

Eckart, C., 1960. Hydrodynamics of Oceans and Atmospheres. Pergamon Press, Oxford.

Eckermann, S.D., 1992. Ray-tracing simulation of the global propagation of inertia gravity waves through the zonally averaged middle atmosphere. J. Geophys. Res.: Atmosphere 97 (D14), 15849–15866. https://doi.org/10.1029/92JD01410.

Eckermann, S.D., 1997. Influence of wave propagation on the Doppler spreading of atmospheric gravity waves. J. Atmos. Sci. 54 (21), 2554–2573.

Eckermann, S.D., Preusse, P., 1999. Global measurements of stratospheric mountain waves from space. Science 286 (5444), 1534–1537. http://science.sciencemag.org/content/286/5444/1534.

Einaudi, F., Hines, C.O., 1970. WKB approximation in application to acoustic-gravity waves. Can. J. Phys. 48, 1458–1471.

Einaudi, F., Bedard Jr., A.J., Finnigan, J.J., 1989. A climatology of gravity waves and other coherent disturbances at the boulder atmospheric observatory during march-april 1984. J. Atmos. Sci. 46 (3), 303–329.

Fovell, R., Durran, D., Holton, J.R., 1992. Numerical simulations of convectively generated stratospheric gravity waves. J. Atmos. Sci. 49 (16), 1427–1442.

Fritts, D.C., Alexander, M.J., 2003. Gravity wave dynamics and effects in the middle atmosphere. Rev. Geophys. 41 (1) paper number 1003. https://doi.org/10.1029/2001RG000106.

Fritts, D.C., Alexander, M.J., 2012. Correction to "gravity wave dynamics and effects in the middle atmosphere". Rev. Geophys. 50 (3) paper number RG3004. https://doi.org/10.1029/2012RG000409.

Fritts, D.C., Smith, R.B., Taylor, M.J., Doyle, J.D., Eckermann, S.D., DÃ¶rnbrack, A., Rapp, M., Williams, B.P., Pautet, P.-D., Bossert, K., Criddle, N.R., Reynolds, C.A., Reinecke, P.A., Uddstrom, M., Revell, M.J., Turner, R., Kaifler, B., Wagner, J.S., Mixa, T., Kruse, C.G., Nugent, A.D., Watson, C.D., Gisinger, S., Smith, S.M., Lieberman, R.S., Laughman, B., Moore, J.J., Brown, W.O., Haggerty, J.A., Rockwell, A., Stossmeister, G.J., Williams, S.F., Hernandez, G., Murphy, D.J., Klekociuk, A.R., Reid, I.M., Ma, J., 2016. The deep propagating gravity wave experiment (DEEPWAVE): an airborne and ground-based exploration of gravity wave propagation and effects from their sources throughout the lower and middle atmosphere. Bull. Am. Meteorol. Soc. 97 (3), 425–453. https://doi.org/10.1175/BAMS-D-14-00269.1.

Fulton, R., Zrnić, D.S., Doviak, R.J., 1990. Initiation of a solitary wave family in the demise of a nocturnal thunderstorm density current. J. Atmos. Sci. 47 (3), 319–337.

Georges, T.M., 1971. A Program for Calculating Three-dimensional Acoustic-gravity ray

Paths in the Atmosphere. Technical Report ERL 212-WPL 16. Natl. Oceanic and Atmos. Admin 43 pp.
Georges, T.M., Jones, R.M., Lawrence, R.S., 1990. A PC Version of the HARPO Ocean Acoustic ray-tracing Program. Tech. Memo ERL WPL-180. Natl. Oceanic and Atmos. Admin, Boulder, Colorado, pp. 18. program available at. http://cires.colorado.edu/~mjones/raytracing/programs.htm.
Gerrard, A.J., Kane, T.J., Eckermann, S.D., Thayer, J.P., 2004. Gravity waves and mesospheric clouds in the summer middle atmosphere: a comparison of lidar measurements and ray modeling of gravity waves over sondrestrom, Greenland. J. Geophys. Res.: Atmosphere 109 (D10). https://agupubs.onlinelibrary.wiley.com/doi/abs/10.1029/2002JD002783.
Gerrard, A.J., Bhattacharya, Y., Thayer, J.P., 2011. Observations of in-situ generated gravity waves during a stratospheric temperature enhancement (ste) event. Atmos. Chem. Phys. 11 (22), 11913–11917. https://www.atmos-chem-phys.net/11/11913/2011/.
Gossard, E.E., Hooke, W.H., 1975. Waves in the Atmosphere. Elsevier Scientific Publishing Company, Amsterdam.
Haase, S.P., Smith, R.K., 1984. Morning glory wave clouds in Oklahoma: a case study. Mon. Weather Rev. 112 (10), 2078–2089.
Hickey, M., Cole, K., 1987. A quartic dispersion equation for internal gravity waves in the thermosphere. J. Atmos. Terr. Phys. 49 (9), 889–899. https://doi.org/10.1016/0021-9169(87)90003-1.
Hickey, M.P., Schubert, G., Walterscheid, R.L., 2009. Propagation of tsunami-driven gravity waves into the thermosphere and ionosphere. J. Geophys. Res. 114, 1–15. https://doi.org/10.1029/2009JA014105. A08304.
Hines, C.O., 1960. Internal atmospheric gravity waves at ionospheric heights. Can. J. Phys. 38, 1441–1481.
Hines, C.O., 1967. On the nature of traveling ionospheric disturbances launched by low-altitude nuclear explosions. J. Geophys. Res. 72 (7), 1877–1882. https://doi.org/10.1029/JZ072i007p01877.
Hoffmann, L., Wu, X., Alexander, M.J., 2018. Satellite observations of stratospheric gravity waves associated with the intensification of tropical cyclones. Geophys. Res. Lett. 45 (3), 1692–1700. https://agupubs.onlinelibrary.wiley.com/doi/abs/10.1002/2017GL076123.
Holton, J.R., Alexander, M.J., 1999. Gravity waves in the mesosphere generated by tropospheric convention. Tellus B 51 (1), 45–58. https://doi.org/10.3402/tellusb.v51i1.16259.
Hung, R., Kuo, J., 1978. Ionospheric observation of gravity-waves associated with hurricane eloise. Journal of Geophysics-Zeitschrift Für Geophysik 45 (1), 67–80.
Hung, R.J., Smith, R.E., 1978. Ray tracing of gravity waves as a possible warning system for tornadic storms and hurricanes. J. Appl. Meteorol. 17 (1), 3–11.
Hung, R.J., Phan, T., Smith, R.E., 1979. Coupling of ionosphere and troposphere during the occurrence of isolated tornadoes on november 20, 1973. J. Geophys. Res.: Space Physics 84 (A4), 1261–1268. https://doi.org/10.1029/JA084iA04p01261.
Hurley, D.G., 1969. The emission of internal waves by vibrating cylinders. J. Fluid Mech. 36 (4), 657672.
Jeffreys, H., 1923. On certain approximate solutions of linear differential equations of the second order. Proc. London, Math. Soc. Ser. 2 23, 428–436.
Jones, W.L., 1969. Ray tracing for internal gravity waves. J. Geophys. Res. 74 (8), 2028–2033. https://doi.org/10.1029/JB074i008p02028.
Jones, R.M., 1996. Three dimensional ray tracing in the atmosphere. In: Dieminger, W., Hartmann, G., Leitinger, R. (Eds.), The Upper Atmosphere. Springer Verlag, Berlin-Heidelberg Ch. II.3.1.4, pp. 307–327, errata available at. http://cires.colorado.edu/~mjones/pubs/errata2.htm, Accessed date: 4 April 2018.
Jones, R.M., 2001. The dispersion relation for internal acoustic-gravity waves in a baroclinic fluid. Phys. Fluids 13, 1274–1280. errata available at. http://cires.colorado.edu/~mjones/pubs/errata9.pdf, Accessed date: 4 April 2018.
Jones, R.M., November 2005. A general dispersion relation for internal gravity waves in the atmosphere or ocean, including baroclinicity, vorticity, and rate of strain. J. Geophys. Res. 110, D22106. https://doi.org/10.1029/2004JD005654. Errata available at. http://cires.colorado.edu/~mjones/pubs/errata7.pdf, Accessed date: 4 April 2018.
Jones, R.M., November 2006. Minimum and maximum propagation frequencies for internal gravity waves. J. Geophys. Res. 111, D06109. https://doi.org/10.1029/2005JD006189. Errata available at. http://cires.colorado.edu/~mjones/pubs/errata8.pdf, Accessed date: 4 April 2018.
Jones, R.M., 2007. Errata: three dimensional ray tracing in the atmosphere. In: Dieminger, W., Hartmann, G., Leitinger, R. (Eds.), The Upper Atmosphere. springer verlag, berlin-heidelberg, pp. 307–327. 1996, 1014 pages, errata available at. http://cires.colorado.edu/~mjones/pubs/errata2.htm, Accessed date: 4 April 2018.
Jones, R.M., 2008a. Errata: a general dispersion relation for internal gravity waves in the atmosphere or ocean, including baroclinicity, vorticity, and rate of strain. J. Geophys. Res. 2005https://doi.org/10.1029/2004JD005654. Errata available at. http://cires.colorado.edu/~mjones/pubs/errata7.pdf, Accessed date: 4 April 2018.
Jones, R.M., 2008b. Errata: minimum and maximum propagation frequencies for internal gravity waves. J. Geophys. Res. 2006https://doi.org/10.1029/2005JD006189. Errata available at. http://cires.colorado.edu/~mjones/pubs/errata8.pdf, Accessed date: 4 April 2018.
Jones, R.M., 2012. Errata: the dispersion relation for internal acoustic-gravity waves in a baroclinic fluid. Phys. Fluids 2001, 1274–1280. Errata available at. http://cires.colorado.edu/~mjones/pubs/errata9.pdf, Accessed date: 4 April 2018.
Jones, R.M., Bedard Jr., A.J., 2015. Infrasonic ray tracing applied to small-scale atmospheric structures: thermal plumes and updrafts/downdrafts. J. Acoust. Soc. Am. 137 (2), 625–632.
Jones, R.M., Riley, J.P., Georges, T.M., 1986a. HARPA - a Versatile Three-dimensional Hamiltonian ray-tracing Program for Acoustic Waves in the Atmosphere above Irregular Terrain. NOAA Special Report, GovDoc No. C55.602:H 18; GPO Item No. 207-C-1; PB87132031. National Oceanic and Atmospheric Administration, Boulder, Colorado, pp. 410. report available at. http://cires.colorado.edu/~mjones/pubs/harpa.pdf, Accessed date: 4 April 2018. http://cires.colorado.edu/~mjones/raytracing.
Jones, R.M., Riley, J.P., Georges, T.M., 1986b. HARPO - a Versatile Three-dimensional Hamiltonian ray-tracing Program for Acoustic Waves in an Ocean with Irregular Bottom. NOAA Special Report, GovDoc No. C55.602:H 23; GPO Item No. 0207-C-01; PB87172573. National Oceanic and Atmospheric Administration, Boulder, Colorado, pp. 455. report available at http://cires.colorado.edu/~mjones/pubs/harpo.pdf (date last viewed 4 April 2018), program available at http://cires.colorado.edu/~mjones/raytracing (date last viewed 4 April 2018).
Jones, R.M., Ostrovsky, L.A., Bedard Jr., A.J., 2017. Ionospheric effects of magneto-acoustic-gravity waves: dispersion relation. J. Atmos. Sol. Terr. Phys. 157–158, 90. https://doi.org/10.1016/j.jastp.2017.04.004.
Jurén, C., Stenflo, L., July, 1973. On resonant interaction of atmospheric waves. Radio Sci. 8 (7), 651–652.
Kim, Y.-J., Eckermann, S.D., Chun, H.-Y., 2003. An overview of the past, present and future of gravitywave drag parametrization for numerical climate and weather prediction models. Atmos.-Ocean 41 (1), 65–98. https://doi.org/10.3137/ao.410105.
Kim, S.-Y., Chun, H.-Y., Wu, D.L., 2009. A study on stratospheric gravity waves generated by Typhoon Ewiniar: numerical simulations and satellite observations. J. Geophys. Res.: Atmosphere 114 (D22). https://agupubs.onlinelibrary.wiley.com/doi/abs/10.1029/2009JD011971.
Knupp, K., 2006. Observational analysis of a gust front to bore to solitary wave transition within an evolving nocturnal boundary layer. J. Atmos. Sci. 63 (8), 2016–2035.
Koch, S.E., Siedlarz, L.M., 1999. Mesoscale gravity waves and their environment in the central United States during STORM-FEST. Mon. Weather Rev. 127 (12), 2854–2879 10.1175/1520-0493(1999)127 < 2854:MGWATE > 2.0.CO;2.
Kramers, H.A., 1926. Wellenmechanik und halbzahlige Quantisierung. Z. Phys. 39, 828–840.
Krisch, I., Preusse, P., Ungermann, J., Dörnbrack, A., Eckermann, S.D., Ern, M., Friedl-Vallon, F., Kaufmann, M., Oelhaf, H., Rapp, M., Strube, C., Riese, M., 2017. First tomographic observations of gravity waves by the infrared limb imager gloria. Atmos. Chem. Phys. 17 (24), 14937–14953. https://www.atmos-chem-phys.net/17/14937/2017/.
Li, X., Zheng, W., Yang, X., Zhang, J.A., Pichel, W.G., Li, Z., 2013. Coexistence of atmospheric gravity waves and boundary layer rolls observed by sar. J. Atmos. Sci. 70 (11), 3448–3459. https://doi.org/10.1175/JAS-D-12-0347.1.
Lighthill, M.J., 1978. Waves in Fluids. Cambridge University Press Cambridge [Eng.], New York. http://www.loc.gov/catdir/toc/cam027/77008174.html.
Lin, Y., Zhang, F., 2008. Tracking gravity waves in baroclinic jet-front systems. J. Atmos. Sci. 65 (7), 2402–2415. https://doi.org/10.1175/2007JAS2482.1.
Liouville, J., 1836. Sur le développement des fonctions ou parties de fonctions en séries dont les divers termes sont assujettis à satisfaire à une même équation différentielle du second ordre contenant un paramètre variable, I. J. Math. Pure Appl. 1, 253–265.
Liouville, J., 1837a. Sur le développement des fonctions ou parties de fonctions en séries dont les divers termes sont assujettis à satisfaire à une même équation différentielle du second ordre contenant un paramètre variable, II. J. Math. Pure Appl. 2, 16–35.
Liouville, J., 1837b. Sur le développement des fonctions ou parties de fonctions en séries dont les divers termes sont assujettis à satisfaire à une même équation différentielle du second ordre contenant un paramètre variable, III. J. Math. Pure Appl. 2, 418–436.
Liu, C.H., Klostermeyer, J., Yeh, K.C., Jones, T.B., Robinson, T., Holt, O., Leitinger, R., Ogawa, T., Sinno, K., Kato, S., Ogawa, T., Bedard, A.J., Kersley, L., 1982. Global dynamic responses of the atmosphere to the eruption of mount st. helens on may 18, 1980. J. Geophys. Res.: Space Physics 87 (A8), 6281–6290. https://doi.org/10.1029/JA087iA08p06281.
Lognonné, P., 2009. Seismic Waves from Atmospheric Sources and Atmospheric/Ionospheric Signatures of Seismic Waves. Springer Netherlands, Dordrecht, pp. 281–304. https://doi.org/10.1007/978-1-4020-9508-5_10.
Lott, F., Millet, C., 2009. The Representation of Gravity Waves in Atmospheric General Circulation Models (GCMs). Springer Netherlands, Dordrecht, pp. 685–699. https://doi.org/10.1007/978-1-4020-9508-5_23.
Ma, J.Z.G., 2016. Atmospheric layers in response to the propagation of gravity waves under nonisothermal, wind-shear, and dissipative conditions. J. Mar. Sci. Eng. 4 (1).
Makela, J.J., Lognonné, P., Hébert, H., Gehrels, T., Rolland, L.M., Allgeyer, S., Kherani, A., Occhipinti, G., Astafyeva, E., Coïsson, P., Loevenbruck, A., Clévédé, E., Kelley, M.C., Lamouroux, J., 2011. Imaging and modeling the ionosphere airglow response over Hawaii to the tsunami generated by the tohoku earthquake of 11 march 2011. Geophys. Res. Lett. 38, 1–5. https://doi.org/10.1029/2011GL047860. L00G02.
Marks, C.J., Eckermann, S.D., Jun. 1995. A three-dimensional nonhydrostatic ray-tracing model for gravity waves: formulation and preliminary results for the middle atmosphere. J. Atmos. Sci. 52, 1959–1984.
McLaren, T.L., Pierce, A.D., Fohl, T., Murphy, B.L., 1973. An investigation of internal gravity waves generated by a buoyancy rising fluid in a stratified medium. J. Fluid Mech. 57 (part 3), 229–240.
Mikumo, T., Watada, S., 2009. Acoustic-gravity Waves from Earthquake Sources. Springer Netherlands, Dordrecht, pp. 263–279. https://doi.org/10.1007/978-1-4020-9508-5_9.
Mowbray, D.E., Rarity, B.S.H., 1967. A theoretical and experimental investigation of the phase configuration of internal waves of small amplitude in a density stratified liquid. J. Fluid Mech. 28 (1), 116.
Muraschko, J., Fruman, M.D., Achatz, U., Hickel, S., Toledo, Y., 2013. On the application of WKB theory for the simulation of the weakly nonlinear dynamics of gravity waves. J. Atmos. Terr. Phys. 90, 1–25.

Nappo, C.J., 2002. An Introduction to Atmospheric Gravity Waves. Academic Press, San Diego.
Nekrasov, A.K., Kurchashov, Y.P., Ivanov, V.N., Pokhotelov, O.A., Bharuthram, R., Shukla, P.K., Stenflo, L., 1992. Dynamics of density irregularities in the e-region of the ionosphere. Phys. Scripta 46 (4), 369. http://stacks.iop.org/1402-4896/46/i=4/a=011.
Nekrasov, A., Shalimov, S., Shukla, P., Stenflo, L., 1995. Nonlinear disturbances in the ionosphere due to acoustic gravity waves. J. Atmos. Terr. Phys. 57 (7), 737–741.
Nicholls, M.E., Pielke, R.A., 1994a. Thermal compression waves. i: total-energy transfer. Q. J. R. Meteorol. Soc. 120 (516), 305–332. https://doi.org/10.1002/qj.49712051605.
Nicholls, M.V.E., Pielke, R.A., 1994b. Thermal compression waves. ii: mass adjustment and vertical transfer of total energy. Q. J. R. Meteorol. Soc. 120 (516), 333–359. https://doi.org/10.1002/qj.49712051606.
NRLMSISE-00, Community Coordinated Modeling Center, 2016. NRLMSISE-00 Atmosphere Model. http://ccmc.gsfc.nasa.gov/modelweb/models/nrlmsise00.php.
Ostrovsky, L.A., 2008. Ionospheric effects of ground motion: the roles of magnetic field and nonlinearity. J. Atmos. Sol. Terr. Phys. 70, 1273–1280.
Plougonven, R., Zhang, F., 2014. Internal gravity waves from atmospheric jets and fronts. Rev. Geophys. 52 (1), 33–76. https://agupubs.onlinelibrary.wiley.com/doi/abs/10.1002/2012RG000419.
Pokhotelov, O.A., Pilipenko, V.A., Fedorov, E.N., Stenflo, L., Shukla, P.K., 1994. Induced electromagnetic turbulence in the ionosphere and the magnetosphere. Phys. Scripta 50 (5), 600. http://stacks.iop.org/1402-4896/50/i=5/a=026.
Pokhotelov, O.A., Feygin, F.Z., Stenflo, L., Shukla, P.K., 1996. Density profile modifications by electromagnetic ion cyclotron wave pressures near the dayside magnetospheric boundary. J. Geophys. Res.: Space Physics 101 (A5), 10827–10833. https://doi.org/10.1029/96JA00543.
Pokhotelov, O.A., Pokhotelov, D.O., Feygin, F.Z., Parrot, M., Kangas, J., Mursula, K., Shukla, P.K., Stenflo, L., 1998. Excitation of helium cyclotron harmonic waves during quiet magnetic conditions. J. Geophys. Res.: Space Physics 103 (A11), 26585–26593. https://doi.org/10.1029/98JA02619.
Pramitha, M., Venkat Ratnam, M., Taori, A., Krishna Murthy, B.V., Pallamraju, D., Vijaya Bhaskar Rao, S., Mar 2015. Evidence for tropospheric wind shear excitation of high-phase-speed gravity waves reaching the mesosphere using the ray-tracing technique. Atmos. Chem. Phys. 15, 2709–2721.
Preusse, P., Eckermann, S.D., Ern, M., 2008. Transparency of the atmosphere to short horizontal wavelength gravity waves. J. Geophys. Res.: Atmosphere 113 (D24) n/a–n/a, d24104. https://doi.org/10.1029/2007JD009682.
Preusse, P., Eckermann, S.D., Ern, M., Oberheide, J., Picard, R.H., Roble, R.G., Riese, M., Russell, J.M., Mlynczak, M.G., 2009. Global ray tracing simulations of the saber gravity wave climatology. J. Geophys. Res.: Atmosphere 114 (D8) d08126. https://doi.org/10.1029/2008JD011214.
Ratcliffe, J.A., 1962. The Magneto-ionic Theory and its Applications to the Ionosphere. University Press, Cambridge.
Rayleigh (John William Strutt), L., 1912. On the propagation of waves through a stratified medium, with special reference to the question of reflection. Proc. Royal Soc. A 86, 207–226.
ReVelle, D.O., 2009. Acoustic-gravity Waves from Impulsive Sources in the Atmosphere. Springer Netherlands, Dordrecht, pp. 305–359. https://doi.org/10.1007/978-1-4020-9508-5_11.
Rolland, L.M., Occhipinti, G., Lognonné, P., Loevenbruck, A., 2010. Ionospheric graity waves detected offshore Hawaii after tsunamis. Geophys. Res. Lett. 37, 1–6. https://doi.org/10.1029/2010GL044479. L17101.
Schoeberl, M.R., 1985. A ray tracing model of gravity wave propagation and breakdown in the middle atmosphere. J. Geophys. Res.: Atmosphere 90 (D5), 7999–8010. https://doi.org/10.1029/JD090iD05p07999.
Šepić, J., Vilibić, I., Rabinovich, A.B., Monserrat, S., 2015. Widespread tsunami-like waves of 23-27 june in the mediterranean and black seas generated by high-altitude atmospheric forcing. Sci. Rep. 5, 11682. https://doi.org/10.1038/srep11682.
Shutts, G.J., 1998. Stationary gravity-wave structure in flows with directional wind shear. Q. J. R. Meteorol. Soc. 124 (549), 1421–1442. https://doi.org/10.1002/qj.49712454905.
Slater, J., Frank, N., 1947. Mechanics. International Series in Pure and Applied Physics. McGraw-Hill Book Company. https://books.google.com/books?id=XOuJnQAACAAJ.
Smith, M.S., 1975. Phase memory in w.k.b. and phase integral solutions of ionospheric propagation problems. Proc. Roy. Soc. Lond.: Mathematical, Physical and Engineering Sciences 346 (1644), 59–79.
Stenflo, L., 1986. Nonlinear equations for acoustic gravity waves. Phys. Scripta 33 (2), 156. http://stacks.iop.org/1402-4896/33/i=2/a=010.
Stenflo, L., 1987. Acoustic solitary vortices. Phys. Fluid. 30 (10), 3297–3299. http://aip.scitation.org/doi/abs/10.1063/1.866458.
Stenflo, L., Jun. 1991. Notizen: acoustic gravity vortices in the atmosphere. Zeitschrift Naturforschung Teil A 46 560–560.
Stenflo, L., 1996. Nonlinear equations for acoustic gravity waves. Phys. Lett. 222 (6), 378–380.
Stenflo, L., Stepanyants, Y.A., Sep 1995. Acoustic-gravity modons in the atmosphere. Ann. Geophys. 13 (9), 973–975. https://doi.org/10.1007/s00585-995-0973-3.
Streltsov, A.V., Chmyrev, V.M., Pokhotelov, O.A., Marchenko, V.A., Stenflo, L., 1990. The formation and nonlinear evolution of convective cells in the auroral plasma. Phys. Scripta 41 (5), 686. http://stacks.iop.org/1402-4896/41/i=5/a=012.
Su, T., Zhai, G., 2017. The role of convectively generated gravity waves on convective initiation: a case study. Mon. Weather Rev. 145 (1), 335–359. https://doi.org/10.1175/MWR-D-16-0196.1.
Suzuki, S., Lübken, F.-J., Baumgarten, G., Kaifler, N., Eixmann, R., Williams, B.P., Nakamura, T., 2013. Vertical propagation of a mesoscale gravity wave from the lower to the upper atmosphere. J. Atmos. Sol. Terr. Phys. 97, 29–36.
Taylor, M., Hapgood, M., 1988. Identification of a thunderstorm as a source of short period gravity waves in the upper atmospheric nightglow emissions. Planet. Space Sci. 36 (10), 975–985. http://www.sciencedirect.com/science/article/pii/0032063388900359.
Testud, J., Nov 1970. Gravity waves generated during magnetic substorms. J. Atmos. Terr. Phys. 32, 1793–1805 Nov 1970.
Tratt, D.M., Hackwell, J.A., Valant-Spaight, B.L., Walterscheid, R.L., Gelinas, L.J., Hecht, J.H., Swenson, C.M., Lampen, C.P., Alexander, M.J., Hoffmann, L., Nolan, D.S., Miller, S.D., Hall, J.L., Atlas, R., Marks, F.D., Partain, P.T., 2018. Ghost: a satellite mission concept for persistent monitoring of stratospheric gravity waves induced by severe storms. Bull. Am. Meteorol. Soc (in press). https://doi.org/10.1175/BAMS-D-17-0064.1.
Tytell, J., Vernon, F., Hedlin, M., de Groot Hedlin, C., Reyes, J., Busby, B., Hafner, K., Eakins, J., 2016. The USArray transportable array as a platform for weather observation and research. Bull. Am. Meteorol. Soc. 97 (4), 603–619. https://doi.org/10.1175/BAMS-D-14-00204.1.
Uccelini, L.W., 1975. A case study of apparent gravity wave initiation of severe convective storms. Mon. Weather Rev. 103 (6), 497–513.
Vadas, S.L., 2007. Horizontal and vertical propagation and dissipation of gravity waves in the thermosphere from lower atmospheric and thermospheric sources. J. Geophys. Res. Space Physics 112 (A6) a06305. https://doi.org/10.1029/2006JA011845.
Vadas, S.L., Fritts, D.C., 2005. Thermospheric responses to gravity waves: influences of increasing viscosity and thermal diffusivity. J. Geophys. Res. Atmos. 110 (D15) d15103. https://doi.org/10.1029/2004JD005574.
Vadas, S.L., Fritts, D.C., 2009. Reconstruction of the gravity wave field from convective plumes via ray tracing. Ann. Geophys. 27 (1), 147–177. http://www.ann-geophys.net/27/147/2009/.
Vadas, S.L., Makela, J.J., Nicolls, M.J., Milliff, R.F., 2015. Excitation of gravity waves by ocean surface wave packets: upward propagation and reconstruction of the thermospheric gravity wave field. J. Geophys. Res.: Space Physics 120 (11), 2015JA021430 9748–9780. https://doi.org/10.1002/2015JA021430.
Volland, H., 1969. The upper atmosphere as a multiply refractive medium for neutral air motions. J. Atmos. Terr. Phys. 31, 491–514.
Wang, Y., Zhang, L., Peng, J., Guan, J., 2017. Mesoscale gravity waves in the mei-yu front system. J. Atmos. Sci. 0 (0) null. https://doi.org/10.1175/JAS-D-17-0012.1.
Weinberg, S., 1962. Eikonal method in magnetohydrodynamics. Phys. Rev. 126, 1899–1909.
Wentzel, G., 1926. Eine Verallgemeinerung der Quantenbedingungen für die Zwecke der Wellenmechanik. Z. Phys. 38, 518–529.
Williams, B.P., White, M.A., Krueger, D.A., She, C.Y., 2002. Observation of a large amplitude wave and inversion layer leading to convective instability in the mesopause region over fort collins, co (41n, 105w). Geophys. Res. Lett. 29 (17) 31–1–31–4, 1850. https://doi.org/10.1029/2001GL014514.
Wrasse, C.M., Nakamura, T., Takahashi, H., Medeiros, A.F., Taylor, M.J., Gobbi, D., Denardini, C.M., Fechine, J., Buriti, R.A., Salatun, A., Suratno, Achmad, E., Admiranto, A.G., 2006. Mesospheric gravity waves observed near equatorial and low-middle latitude stations: wave characteristics and reverse ray tracing results. Ann. Geophys. 24 (12), 3229–3240. https://www.ann-geophys.net/24/3229/2006/.
Zhang, D.-L., Fritsch, J.M., 1988. Numerical simulation of the meso-β scale structure and evolution of the 1977 Johnstown Flood. Part III. Internal gravity waves and the squall line. J. Atmos. Sci. 45 (7), 1252–1268.
Zhao, J., Chu, X., Chen, C., Lu, X., Fong, W., Yu, Z., Jones, R.M., Roberts, B.R., Dörnbrack, A., 2017. Lidar observations of stratospheric gravity waves from 2011 to 2015 at McMurdo (77.84°S, 166.69°E), Antarctica: Part I. Vertical wavelengths, periods, and frequency and vertical wave number spectra. J. Geophys. Res.: Atmosphere 122 (10), 2016JD026368 5041–5062. https://doi.org/10.1002/2016JD026368.